WIDE FIELD OF VIEW IMAGING OF PREMOTOR AND SENSORIMOTOR CORTEX

ACTIVATION PATTERNS BY FUNCTIONAL

NEAR INFRARED SPECTROSCOPY

by

PANKAJ CHAND

Presented to the Faculty of the Graduate School of

The University of Texas at Arlington in Partial Fulfillment

of the Requirements

for the Degree of

MASTER OF SCIENCE IN BIOMEDICAL ENGINEERING

THE UNIVERSITY OF TEXAS AT ARLINGTON

December 2010

ACKNOWLEDGEMENTS

ABSTRACT

WIDE FIELD OF VIEW IMAGING OF PREMOTOR AND SENSORIMOTOR CORTEX

ACTIVATION PATTERNS BY FUNCTIONAL

NEAR INFRARED SPECTROSCOPY

Pankaj Chand, M.S.

The University of Texas at Arlington, 2010

Supervising Professor: Georgios Alexandrakis

Functional near infrared spectroscopy (fNIRS) is a non-invasive optical technique which can measure concentration changes of oxygenated (HbO), deoxygenated (HbR), and total hemoglobin (HbT) in brain tissue that are induced by neuronal activation. A major hindrance at present for brain optical imaging research is the limited field of view (FOV) size, which is restricted due to the limited number of source-detector pairs that current fNIRS hardware technology and cost considerations allow. As a result it is challenging to simultaneously capture hemodynamic changes in the premotor, motor and sensory cortex as some of these activations can occur outside the available FOV.

My research focuses on the design of a new probe holder assembly for the DYNOT (NIRx Inc.) fNIRS imaging system which enables larger FOV imaging that encompasses the premotor, motor and sensory cortex regions. The probe holder assembly consists of (a) a portable stand that supports the weight of optical fiber bundles up to a few centimeters above the head's surface and (b) a pliable probe holder that guides the fiber bundles onto the head's

surface and ensures good optical contact with the scalp. The pliable probe holder consists of a sandwich of several different layers of materials that were chosen to attain a reasonable compromise between the requirement for flexibility to fit well onto the scalp and for rigidity to hold stably the source-detector fiber bundles vertically onto the head's surface. The portable stand significantly alleviates the problem of the DYNOT's fiber bundles heavy weight that created comfort issues for the subjects being imaged. Therefore the maximum available number of source-detector pairs could be used, which enabled imaging over a larger FOV without affecting subject comfort. The probe holder fixed the placement of DYNOT's bifurcated source-detector fiber bundles on a regular spacing arrangement that kept nearest neighbors at a distance of 2.2 cm and next-nearest neighbors at a distance of 3.2 cm. As a result, in the current study 32 source-detector pairs were used that covered 8.4 x 12 cm area spanning the premotor, motor and sensory cortex.

Having established a larger FOV we evaluated how different hand and arm motions activated different premotor, motor and sensory areas. More specifically, we employed activations protocols entailing group finger tapping, sequential finger tapping, squeezing a soft ball and flipping cards form a deck. We also used a purely sensory stimulation protocol as a control. These protocols enabled us to study differences in timing and localization of activation in different cortical regions, as elicited from each task. We present results for each of these activation protocols for three subjects. In addition, we have also studied the resting state connectivity for seed locations corresponding to the maximum activation locations in premotor, motor and sensory cortical regions, as identified during performance of the activation protocols. We also present the use of a spatiotemporal clustering algorithm that was adapted from the functional Magnetic Resonance Imaging (fMRI) literature to assess the physical size of activation/deactivation regions for each of these protocols in a quantitative fashion. The results

from this clustering analysis indicate that different cortical activation regions are physically adjacent, a fact that is not evident from visual inspection of the activation images.

This work presents for the first time, to our knowledge, activation images over a FOV that is larger than was previously reported, thus enabling simultaneous observation of spatiotemporal activation patterns in different cortical regions during performance of activation protocols. Future developments such as the outfitting of the DYNOT source-detector fiber bundles with brush-like optical fibers will enable improved comfort and optical contact during measurements, which can be very helpful for other clinical uses.

TABLE OF CONTENTS

LIST OF ILLUSTRATIONS

CHAPTER 1

INTRODUCTION

1.1 Principles of FNIRS

1.1.1 Diffuse Optical Imaging

Functional near-infrared spectroscopy (fNIRS) is a noninvasive spectroscopic method that uses near-infrared light to measure changes in the concentrations of oxyhemoglobin [HbO] and deoxyhemoglobin [HbR] in the human brain resulting from neuronal activation. The wavelength range of near-infrared light is 600 nm - 900 nm, which belongs to a region of the electromagnetic spectrum that spans from deep red to wavelengths that are slightly beyond those that the human eye can see (Figure 1.1) [1].
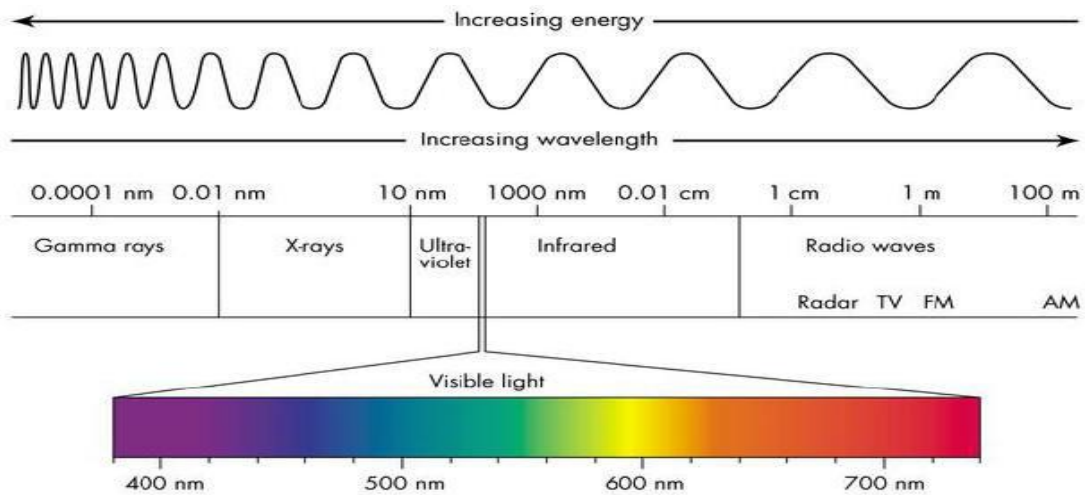
Figure 1.1: Electromagnetic Spectrum [2]

Most biological tissues are relatively transparent to light in the near-infrared range, which is usually called the "optical window". This is mainly due to the fact that within this optical

1

window,the absorbance of the main constituents in the human tissue (i.e. water, oxy-Hb, and deoxy-Hb) is small, permitting the light to penetrate deeper into the brain.
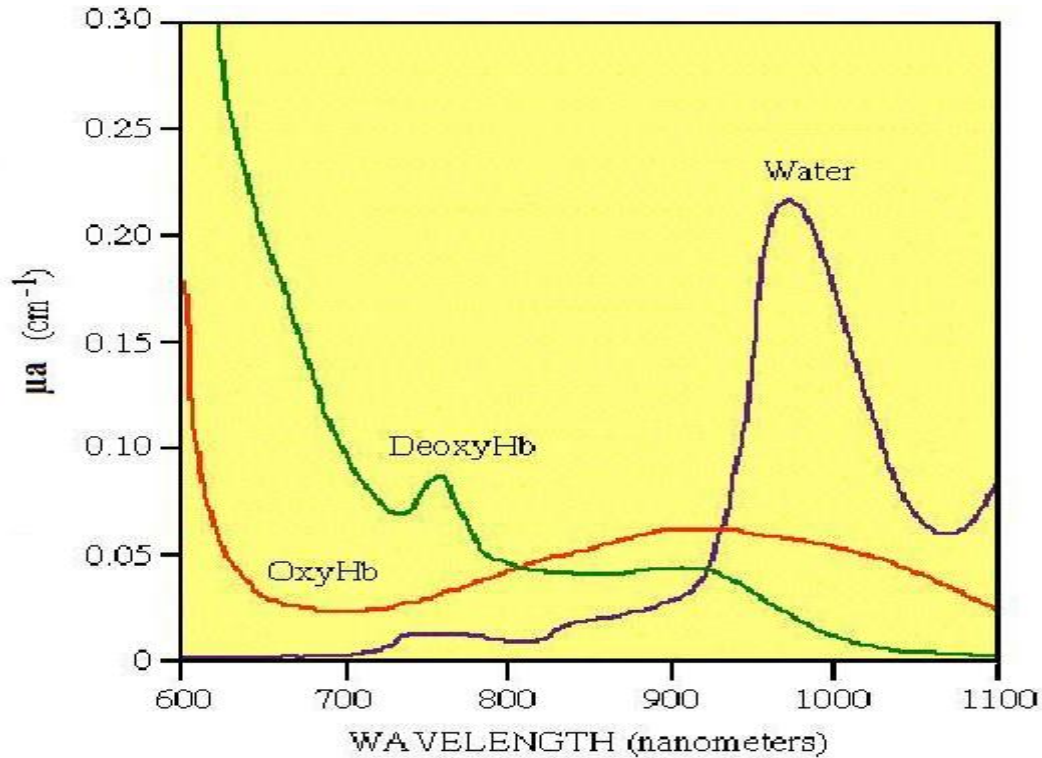
Figure 1.2: Absorption Spectra of HbO, Hb, and Water [4].

In fNIRS imaging, near-infrared light is introduced into the head by optical fiber bundles and after propagating through the dense scattering layers of the scalp and skull into the brain (Figure 1.3) it is collected by other fiber bundles that are also placed on the scalp surface. Changes in oxy- and deoxyhemoglobin concentrations, i.e. [HbO] and [Hb] (also abbreviated as [HbR]) respectively, in the vicinity of neuronal activation regions affect directly the amount of near-infrared light absorption and therefore the light intensity detected on the surface of the scalp. As the activation hemodynamics is time-dependent, so is the variation of the detected light intensity.
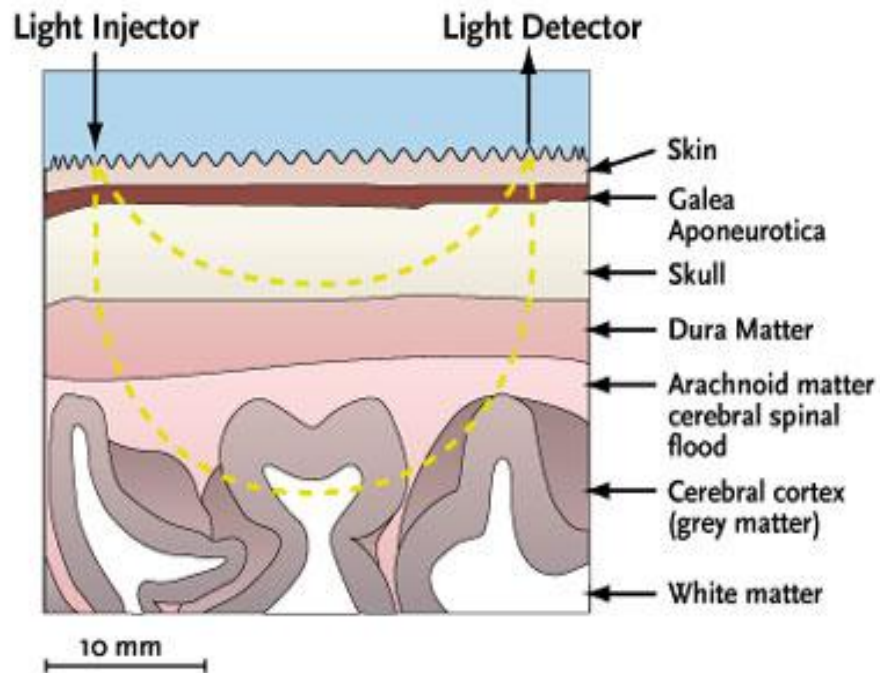
Figure1.3: Photon Path Travelled Inside the Brain [26]

The subject is asked to perform a specific task that activates the cortical region of the brain under study following a prescribed activation protocol, e.g. finger tapping to activate the sensory-motor cortex. While this protocol is being performed the activated neurons require oxygen and nutrients, the supply of which is regulated by a physiological process known as neurovascular coupling [25].

Neurovascular coupling can be defined as the relation between local neural activity and consequent changes in cerebral blood flow (CBF) and oxy- deoxy hemoglobin concentrations. The magnitude and spatial location of blood flow and oxygen saturation (defined as [HbO]/([HbR]+[HbO]) changes are strongly linked to changes in neural activity via complex sequence of corresponding events involving glia, neurons, and vascular cells [25],[46].

Functional brain imaging techniques that can quantify hemodynamics changes, such as functional magnetic resonance imaging (fMRI) and fNIRS, rely on the modeling of neurovascular coupling to understand the underlying changes in neural activity that occurs at shorter time scales [25,46].
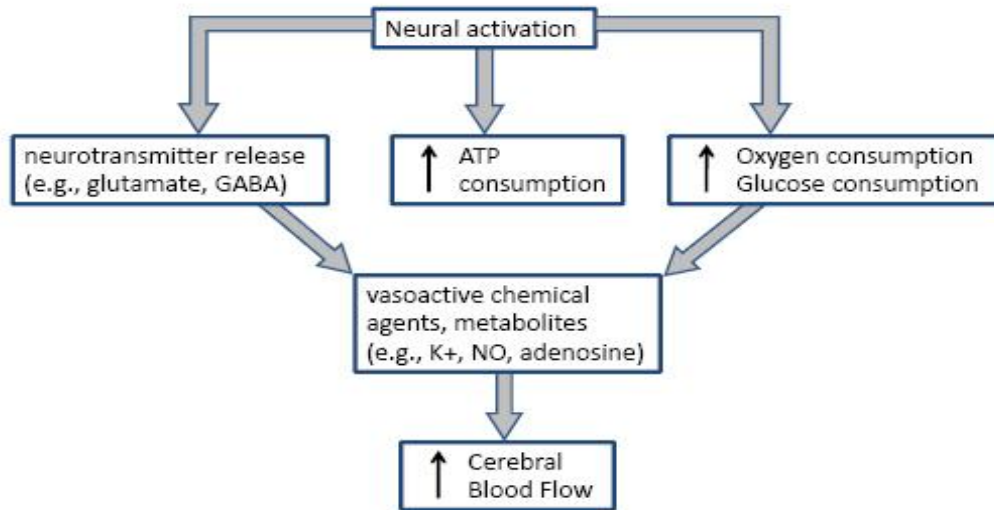
Figure 1.4: Neurovascular Coupling [25]

Furthermore, time-dependent variations of the light signal can be induced by physiological hemodynamics, namely cardiac pulsation, respiration and Mayer waves, which are unrelated to the activation process [47]. The amplitude of these hemodynamic signals is large compared to activation amplitudes and the frequency range of respiration and Mayer waves may overlap with those of activation-related [48]. To remove the confounding effects of physiological interference a number of filtering techniques such as PCA and adaptive filtering have been used [49]. In this work we have performed a combination of PCA and adaptive filtering which will be described in the Methods Section in Chapter 2.

1.1.2 Modified Beer Lambert's Law

When the near infra-red light enters the human brain it undergoes absorption and scattering and is quantified by the respective absorption (μ_a) and reduced scattering (μ_s') coefficients.

The μ_a determines how far into a material light of a particular wavelength can penetrate before it is absorbed and is defined by:

$$\mu_a = 2.3 * \varepsilon * C, \qquad\qquad (Eq1)$$

where $\varepsilon(mMol^{-1}\ cm^{-1})$ is the wavelength-dependent molar absorptivity coefficient, and $C(M)$ is the concentration of the absorbing substance. As the dominant tissue chromophores in the optical window are Hb and HbO, μ_a is expressed as a sum of the contribution of both of these to the total absorption. The units of μ_a are cm^{-1}[28].

Scattering in optically thick media can be characterized by two parameters, i.e., the scattering coefficient (μ_s) and the scattering anisotropy (g). The μ_s is a measure of the mean scattering length (inversely proportional to mean free path), l_s, between two scattering events[29].

$$L_s = 1/\mu_s \qquad\qquad (Eq2)$$

Scattering anisotropy factor (g) is the mean cosine of the scattering angle between the incident and scattered light direction. [30]

$$i.e.,\ g= <\cos \theta > \qquad\qquad (Eq3)$$

The reduced scattering coefficient μ_s' is an equivalent measure of the mean free path (mfp) traveled between two isotropic light scatterers:

$$L= 1/\mu_s' \qquad\qquad (Eq\ 4)$$

where, $\mu_s' = \mu_s(1 - g)\ [cm^{-1}]$

The change in light absorption is known as delta optical density, ΔOD, can be calculated from the normalized changes in the light incident on a detector from a source position.

Formally, ΔOD is defined as

$$\widehat{\Phi}_{ij}^{\lambda}(t) = \int_{r(\gamma)} \widehat{\Phi}_{ij}^{\lambda}(0) e^{-\Delta\mu^{\lambda}{}_{abs}(\vec{r})} \cdot d\,\vec{r},$$

(Eq 5)

$$\Delta OD^{\lambda}{}_{ij}(t) = Ln\left[\frac{\widehat{\Phi}_{ij}^{\lambda}(0)}{\widehat{\Phi}_{ij}^{\lambda}(t)}\right],$$

(Eq 6)

where Φ_{ij} (intensity) is the amount of light emitted from a source position (i) that is incident on a given detector position (j). $\Delta\mu_{abs}$ is the change in the absorption coefficient with respect to the baseline level. These changes are specific to the wavelength of light examined, which is indexed by λ. The spatial integrals in Eqs. (5) are functional path integrals over the volume sampled by the ensemble of possible photon trajectories through the tissue, which in turn is defined by the stochastic diffusion of light in tissue [42]. In other words we can say that the detected light intensity is proportional to the amplitude of the voltage signal reported by the photon detectors, as long as these are not near saturation.

For most optical functional brain measurements, hemoglobin absorption changes related to neuronal activation are considered to be small compared to baseline and thus are thought to not disturb the path of light through the tissue. For a typical vascular change due to brain activation (around 1–5 μM in oxyhemoglobin), the expected change in optical density is

6

0.1%–1.0% cm^{-1}. In this limit, absorption changes can be expressed as a linear combination of the changes in oxyhemoglobin (HbO_2) and deoxyhemoglobin (HbR), by replacing the path integral in Eq. (5) with the multiplication by an effective mean path-length term that depicts the average path of light traveled through the illuminated region [42]. The final resulting linear relationship between changes in optical density and changes in the underlying concentration of absorbing chromophores in the sample is called as the Beer–Lambert law:

$$\Delta OD_{ij}{}^{\lambda} = L_{ij}{}^{\lambda}(\varepsilon_{HbR}^{\lambda}\Delta[HbR] + \varepsilon_{HbO_2}^{\lambda}\Delta[HbO_2]),$$

(Eq7)

where the variable ε is the wavelength-dependent extinction coefficient for each hemoglobin species. In Eq. (7), L_{ij} is the mean path length traveled by the light from the source i to the detector j.

Since light propagation through biological tissue follows a diffuse rather than a straight path, the Beer–Lambert law must be adjusted for the additional effective distance traveled by light as it scatters through the tissue. Also, since the tissue region where the absorption is presumed to be changing (e.g., the brain) is only a small fraction of the volume that the diffuse light samples, partial volume corrections must also be applied to rescale the magnitude of absorption changes. The combination of path length and partial volume scaling can be included into a term denoted by the differential path-length factor (DPF) within the modified Beer–Lambert Law (MBLL) [51,52]. The net absorption change at each wavelength due to changes in hemoglobin concentration is specified by the following equation

$$\Delta OD_{ij}{}^{\lambda} = L_{ij}{}^{\lambda}DPE^{\lambda}(\varepsilon_{HbR}^{\lambda}\Delta[HbR] + \varepsilon_{HbO_2}^{\lambda}\Delta[HbO_2]),$$

(Eq 8)

In the above equation, the term DPF (differential path-length factor) has been added to account for differences between the linear distance between the source and detector pair (L_{ij})

7

and the true effective mean path length that light travels as it scatters through the tissue. This term has wavelength dependence, because the effective mean path length depends on the scattering properties of the illuminated tissue. To calculate the approximate change in optical density related to brain activity, one must also account for partial volume scaling due to the fact that hemoglobin changes are not equally distributed along the illuminated tissue but are limited to a restricted cortical volume. This partial volume effect results in an underestimation of the effective hemoglobin changes in the cortex. The effects of scattering and partial volume can be accounted for by multiplying the linear source–detector separation by additional differential and partial path-length factors. This scaling factors adjust for the effective path length of light through the region of interest by approximating that all absorption changes occurs within a subset of the total sampled volume [42].

In most fNIRS brain activation studies, multiple wavelength measurements of optical absorption are often transformed to changes in oxyhemoglobin and deoxyhemoglobin by solving the series of linear equations posed by the MBLL. Hemoglobin changes can be estimated by a minimum weighted least-squares solution to Eq. (8) from data at two or more wavelengths. This is given by the equation

$$
\begin{bmatrix} \Delta[\mathrm{HbO_2}] \\ \Delta[\mathrm{HbR}] \end{bmatrix} = (\mathbf{E}^T \mathbf{R}^{-1} \mathbf{E})^{-1} \mathbf{E}^T \mathbf{R}^{-1} \begin{bmatrix} \Delta\mathrm{OD}^{\lambda_1}/L^{\lambda_1}\mathrm{DPF}^{\lambda_1} \\ \vdots \\ \Delta\mathrm{OD}^{\lambda_N}/L^{\lambda_N}\mathrm{DPF}^{\lambda_N} \end{bmatrix},
$$

(Eq 9)

where

$$
\mathbf{E} = \begin{bmatrix} \varepsilon^{\lambda_1}_{\mathrm{HbO_2}} & \varepsilon^{\lambda_1}_{\mathrm{HbR}} \\ \vdots & \vdots \\ \varepsilon^{\lambda_N}_{\mathrm{HbO_2}} & \varepsilon^{\lambda_N}_{\mathrm{HbR}} \end{bmatrix}.
$$

(Eq 10)

8

The matrix E contains the extinction coefficients for oxyhemoglobin and deoxyhemoglobin at each wavelength measured. In Eqs. (9 and 10), the matrix R is the *a priori* estimate of the covariance of the measurement error. This equation arises from a weighted least-squares cost function, and the effect of normalization by this measurement error term is to precondition the measurements by weighting according to their expected measurement noise levels. There may not be a unique solution of the MBLL that simultaneously satisfies all measurements [42].

1.2 Brain Physiology

The human brain is the center of the human nervous system. It is mainly divided into brainstem, cerebellum and cerebrum. The cerebrum is the largest part of brain which is compartmentalized so that different regions have different functions.
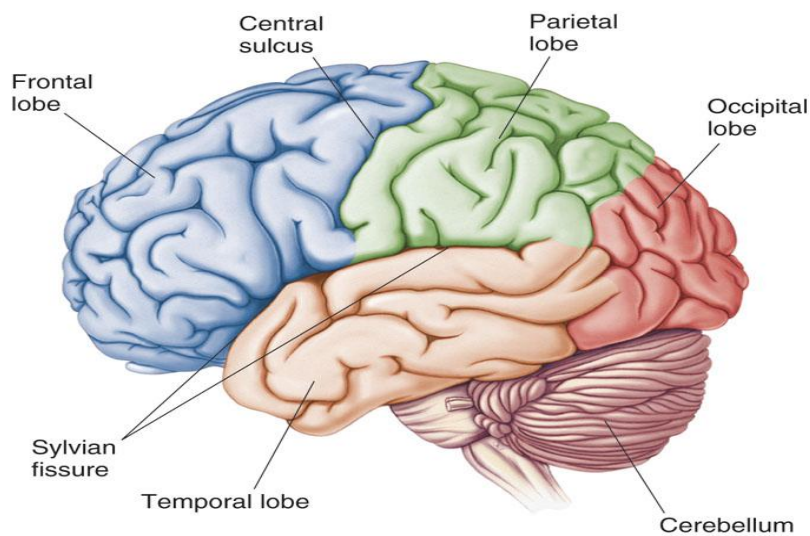
Figure 1.5: The Lobes of the Human Brain [20].

As shown in Figure 1.4 the brain is mainly divided into four lobes - the frontal, parietal, occipital and temporal lobe. The frontal lobe plays a major role in the planning and execution of movements. The temporal lobe is vital for language. The parietal lobe is responsible for somatosensation and receives inputs from the somatosensory relays of the thalamus and

represents information concerning touch, pain, temperature, and limb proprioception. The occipital lobe is dedicated to visual processing and although it is of enormous interest for neuroscience, it does not play an important role in language, aside from its essential role in reading and in the various semiological phenomena involved in visual perception [32].

The cerebral cortex is specialized into sensory areas for perception, motor areas that direct movement and association areas that integrate information as shown in Figure 1.5. The focus of the fNIRS measurements performed in this work is to explore the spatiotemporal hemodynamic activation patterns elicited in these regions as a result of different arm and hand motions.
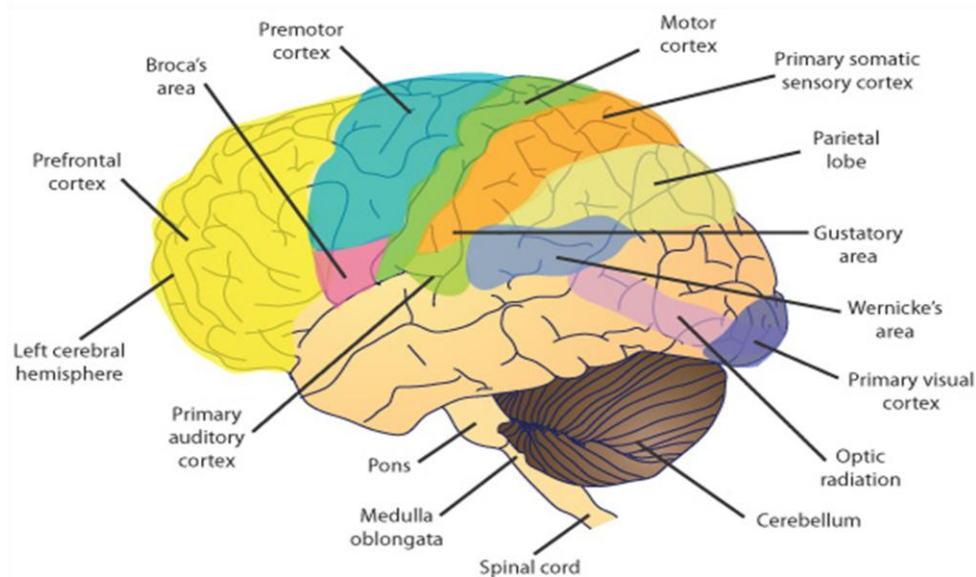
Figure 1.6: Human Brain Anatomies [10]

1.2.1 Premotor Cortex

As depicted in Figure 1.5 the premotor cortex lays in front lobe of the brain. The premotor cortex plays a critical role in sensory guidance of movement and control of proximal and trunk muscles of the body. Whenever we perform a complex motor movement like sequential taping the task is carried out by neural circuitry in the premotor cortex, circuitry

connected via neural bindings to the appropriate synergies in the motor cortex. The premotor cortex is further broadly classified into medial and lateral premotor cortex. The medial premotor area is responsible for coordination of sequential tasks. The medial premotor area is also called supplementary motor area (SMA) or motor association cortex. The lateral premotor cortex is responsible for complex movement like association of a new visual cue with the movement [21].

1.2.2 Primary Motor Cortex

The motor cortex is located in the rear portion of the frontal lobe, just before the central sulcus (furrow) that separates the frontal lobe from the parietal lobe as shown in Figure 1.5. Area 4, also known as the primary motor cortex, forms a thin band along the central sulcus. The primary motor cortex controls all the voluntary movements of the body [22]. It sends impulses to lower parts of the body via the spinal cord, and during complex tasks it coordinates movements with help from the premotor cortex.

As Shown in Figure 1.6 every part of the body is represented in the primary motor cortex, and these representations are arranged somatotopically. There are unequal amounts of cortical areas devoted to movements of all the body parts in motor cortex [24].

1.2.3 Sensory Cortex

The sensory cortex lies in the parietal lobe of the brain and it is involved in processing tactile information, heat and cold sensitivity. The sensory cortex receives sensory information from the skin, muscoskeletal system, viscera, and taste buds. There are sensory receptors, neural pathways, and parts of the brain involved in sensory perception.

11
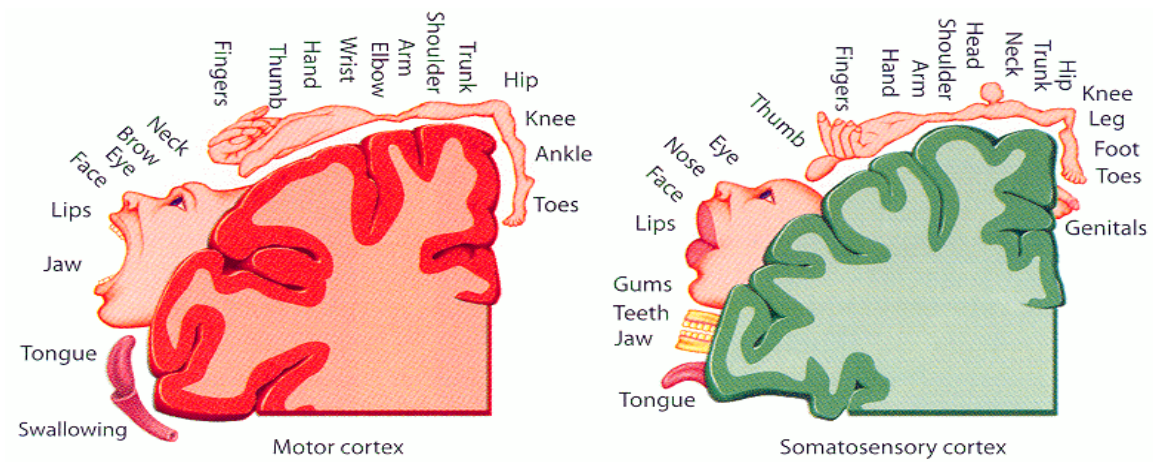
Figure 1.7: The Primary Motor and Sensory Homunculus in cerebral cortex [23]

1.3 Previous Work

A large number of experiments have been performed in the field of cortical activation studies in last two decades. Several types of brain activity like motor, sensory and cognitive activities have been assessed by fNIRS [23, 24, 27, 53]. These studies were performed with single- or two-channel instruments, whereas recent studies have also been carried out with multichannel fNIRS instruments [27].

The development of multichannel continuous wave imaging systems also increased the FOV but the cortical studies faced a major obstacle as the increased FOV size was still insufficient to study activations over the whole brain surface.

In recent years the use of commercially available fNIRS continuous wave imaging systems like the CW4, CW5, CW6 and DYNOT has greatly facilitated the use of fNIRS as a way to quantify cortical activation patterns under a variety of different paradigms. A recent successful attempt in using a multichannel continuous fNIRS system in 2005 involved the use of a probe assembly consisting of 8 detectors and 4 sources with a uniform separation of 2.9 cm. [1, 12]. This probe assembly was positioned approximately over the subject's contra-lateral

primary motor cortex. The protocol used was an event-related finger-tapping task in which subject is asked to tap for fixed time followed by rest which is repeated for 4-5 blocks which resulted in the expected hemodynamic changes in the primary motor cortex. The major obstacle faced in this experiment was limited number of source detector pairs [12].

In another recent attempt in 2003 cognitive brain activation study over a wider FOV; probes of a Hitachi NIRS system were placed on a subject's frontal and bilateral temporal regions. In this study two 24-channel NIRS systems were used and the inter-optode distance was 3 cm. The total FOV size was 8 x 8 cm. The cognitive activation protocol consisted of a 30-s pre-task baseline, a 60-s word fluency task, and a 60-s post-task baseline. The biggest limitation of this study was that two NIRS machines were used and the coverage area was not enough to cover more areas of brain [36].

A somewhat more recent (2005) successful attempt in using a multichannel continuous CW4 fNIRS system which involved the use of a probe assembly consisting of 8 detectors and 4 sources with a uniform separation of 2.9 cm [12]. This probe assembly was positioned approximately over the subject's contralateral primary motor cortex making a total FOV size of 8.7 x 5.8 cm. The protocol used was an event-related finger tapping task in which subject was asked to tap for a fixed time followed by rest which was repeated for 4-5 blocks and resulted in the expected hemodynamic changes in the primary motor cortex. The major obstacle faced in this experiment was limited number of source-detector pairs [12].

In another study (2004) using a CW5 system with 16 sources and 32 detectors, a number of different protocols (finger tapping, cognitive and visual tasks) were used to activate prefrontal, sensorimotor and visual cortical areas. The minimum source-detector distance separation used was 3 cm. By arranging source-detectors in a sparse pattern these investigators were able collect fNIRS signals over the largest cortical area studied by fNIRS to date, which spanned all of the aforementioned cortical areas. However, possibly due to the

13

sparseness of the source-detector arrangement, only signals from the channels with the strongest signals were reported, but no activation images were created [33].

Recently some efforts have been made in covering extended areas of the brain. In a recent study (2007 – 2009) of the sensory-motor cortex a Cephalogics high density NIRS system was employed with 24 sources and 18 detectors. In addition, visual cortex activation was also studied using a similar source-detector arrangement. The first nearest neighbor distance used was 13 mm, and the second nearest neighbor distance was 30 mm. The biggest limitation of this study was in order to make a high density source detector configuration the investigators had to trade off with the FOV size [16].

This year in June 2010 another semotosensory study was done using DYNOT system. The optical probes form a rectangular array of 30 fibers with inter-optode distance of 0.75 cm. The total FOV was 3.75 x 3 cm. Finger tapping and vibrotactile protocols were used in the experiments. The results were co-registered to the individual anatomical brain anatomy (MRI) which confirmed the localization in the expected cortical gyri in the subjects. We demonstrated that high-density optical imaging allows for a fine-grained resolution of functional cortical activations in the pericentral motor and somatosensory cortices[58].

1.4 The Current Work

In this work we have used an fNIRS imaging system (DYNOT, NIRx Inc) employing an array of bifurcated source-detector fiber bundles to image cortical activation over a FOV, spanning the premotor, primary motor and somatosensory cortex. A compromise was made such that only one hemisphere of the cortex was imaged due to the limited number of source-detector pairs available. The problem of high fiber bundle weight was significantly alleviated through construction of a support structure, which made fNIRS data acquisition possible without discomfort for the subjects. This work presents, to our knowledge for the first time, fNIRS

14

images over an extended FOV (8.4 x 12 cm) in a single brain hemisphere for a number of different hand and arm motion activation protocols. The unique spatio-temporal relation of premotor, motor and sensory activation patterns for each type of movement is demonstrated. As such, the activation protocols presented here can be thought of as recipes of how to elicit activation from specific cortical regions. In addition, application of a spatiotemporal clustering algorithm to these fNIRS images demonstrates that the activation regions are larger than is perceived by direct observation of activation images and that these activation regions are in fact physically adjacent [34].

CHAPTER 2

MATERIALS AND METHODS

2.1 The Dynamic Near-Infrared Optical Tomography DYNOT Imaging System

The DYNOT system uses a noninvasive functional imaging method that employs low-energetic laser radiation to probe highly scattering media, such as tissue. The term dynamic is used because multiple optical tomographic data sets are acquired in a continuous fashion at high repetition rates (several images per second), thus allowing the study of physiologic changes inside the target. In this system, two wavelengths (760 nm and 830 nm) are provided by two laser diodes, whose light is coupled sequentially into 32 different fiber bundles that deliver the light to various positions on the surface of the tissue to be studied. Each laser is operated at an output power of about 100 mW; about 25 mW of which reaches the target. The laser intensity is a sine-wave modulated at a frequency in 4-11 kHz range [17, 18].

Figure 2.1: The DYNOT imaging system [19]

16

Each source fiber bundle forms one branch of a bifurcated fiber bundle that joins another branch. This second branch is used for light detection. Each detector fiber bundle terminates on a single silicon photodiode of a multi-channel detection module [18].
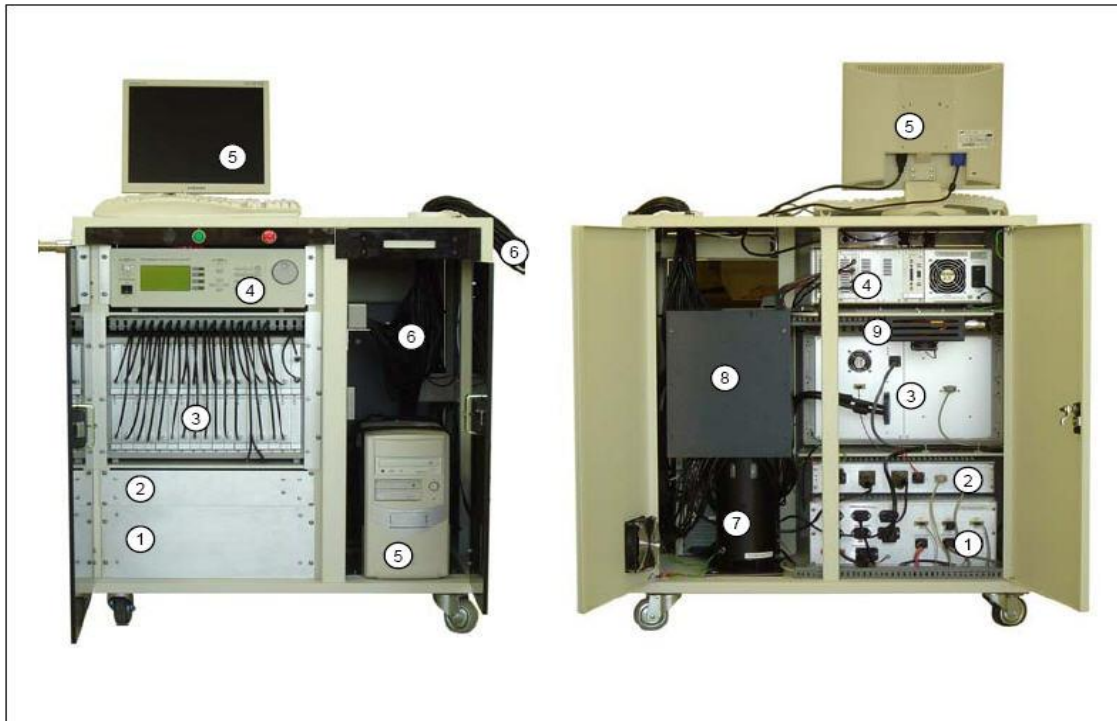
Figure 2.2: Front (left) and back (right) view of the DYNOT instrument [19].

The host computer governs the communication between the various system hardware components and data acquisition. The DYNOT system is operated using a MS Windows-based GUI (dynaSCAN), which provides an interactive virtual control panel on the host PC [19].

The front and back view of the DYNOT system is shown in Figure 2.2, with labels for the various subsections. The various subsections are:

1 – Power supply,

2 – Motor controller,

3 – PMD (programmable multi-channel detector) with detection fibers,

4 – Laser diode controller,

5 – PC with monitor/keyboard,

6 – Fiber optic cables,

7 – Optical switch,

8 – Optics shielding cover,

9 – Laser diodes (covered).
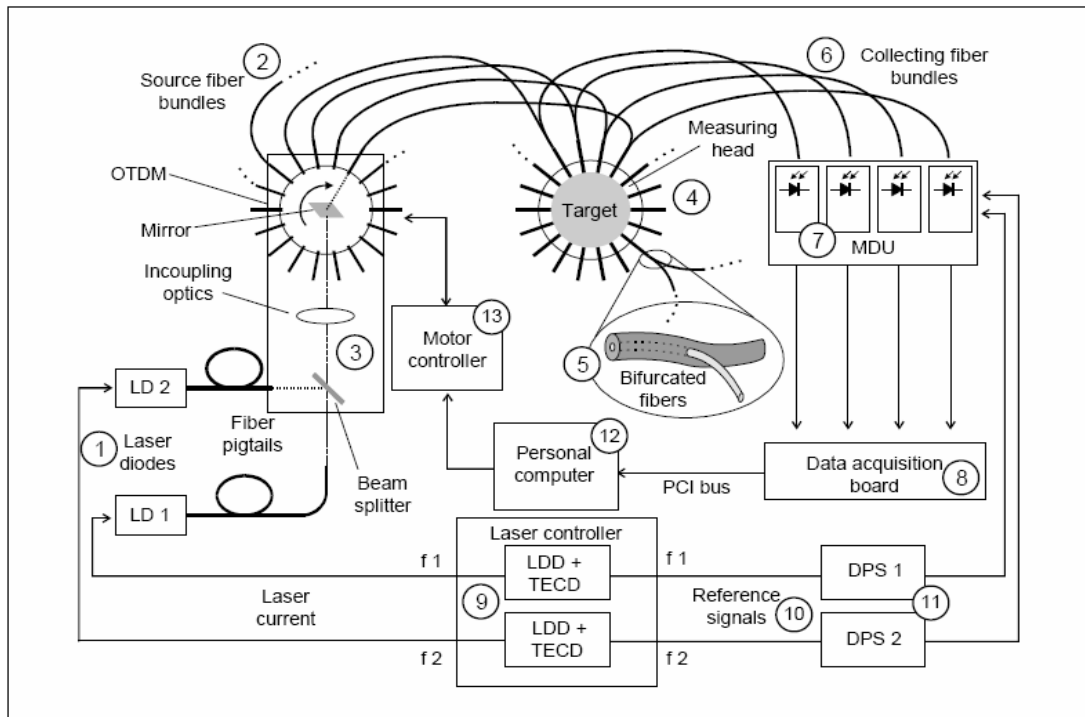
Figure 2.3: Block diagram for DYNOT instrument [19].

In Figure 2.3 block diagram of DYNOT machine is shown where the following stands for, LD: laser diodes, LDD: laser diode driver, f 1, 2: laser modulation frequencies, TECD: thermo-electric cooler driver DPS: digital phase shifter, OS: optical time-division multiplexer.

Initially light from two laser diodes (1) is combined and focused into an optical switch (3). Light is sequentially deflected on to each of the source fiber with the help of a rotating mirror within the optical switch (3). The DC servo motor controls the mirror movement under the control of a computer operated motor controller (13). Fiber bundles (6) consists of 32 bifurcated fibers, which serves the purpose of guiding the source light to the target and the back reflected light from the target to a programmable multi-channel detector (PMD) (7). The data acquisition board (8) digitizes the output from PMDs. Laser controller (9) controls the operation and temperature-stabilization of the laser diodes.

2.2 Design of a New Probe Holder to Alleviate Fiber Bundle Weight

2.1.1. The new probe holder

To increase the FOV size we designed a new probe holder that spans the areas premotor, motor and sensory cortex while supporting the weight of all fiber bundles so that subjects do not feel discomfort from the pressure of these fibers on the scalp. The probe holder consists of a sandwich of three layers of different materials so as to keep a balance between the necessary rigidity for holding the probe tips steady and the flexibility needed to accommodate the curvature of the head. The materials were also selected on the basis of weight and comfort for the subjects.

(a)

(b)
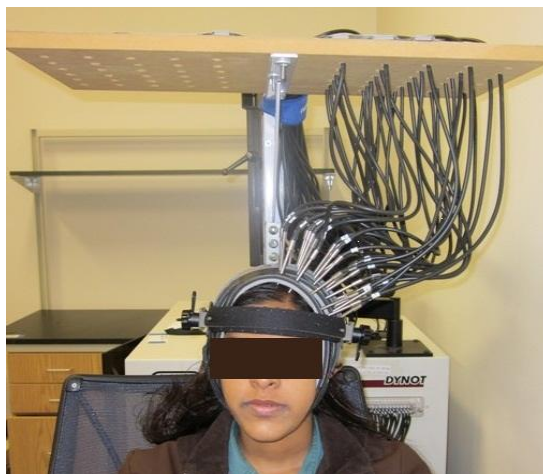
(c)

Figure 2.4: New Probe Holder Setup (a) Probe Holder, (b) Probe Headband
(c) Probe Holder on the Subject's Head

The following materials were used in order to make the new probe holder (Fig. 2.4 (a)):

(1) Hard self stick vinyl rubber (Roppe Corporation): It is the outermost layer of the probe holder. Self stick hard vinyl rubber material was used as it gives rigidity to the probe holder. Rigidity is one of the most crucial factors in designing the probe holder because if the probe holder is not rigid enough the fiber bundles can fall off, or the optical contact will not be good enough, leading to poor data quality.

(2) Buna Rubber (Ace Hose & Rubbber Co.): This comprises the middle layer of the probe holder which is very flexible. As the outermost layer of the probe holder is thin, this middle layer provides the required thickness to the probe holder holes so that they can hold up vertically the long fiber bundles onto the scalp.

(3) Self Adhesive Foam (Patterson Medical): In order to make probe holder comfortable, foam is used as the innermost layer, which touches the head.

(4) Plastic Head Band (BKR): In order to attain maximal optical contact with the scalp some mild pressure needs to be applied on this 3-layer assembly by a head band (Fig. 2.4(b)), so that the probe holder can stay comfortably but steadily onto the subject's head (Fig. 2.4(c)).

The setup time for the probe holder was 15 min which included positioning on the scalp, and securing the assembly with a headband running from ear to ear and Velcro straps running under the chin. Subject 1 and Subject 3 had previously been subjects of fNIRS measurements performed with the DYNOT system using the commercially available probe holders for the system, while Subject 2 had no such prior experience.   The individual comments of all the three subjects regarding the comfort of the probe holder are as follows:

Subject 1: "The comfort level of the newly designed probe holder is very good as compared to the earlier probe holder, which was very heavy and gave headaches in first 20 -30 minutes of

21

use. This discomfort made it impossible to perform several experiments sequentially on the same day."

Subject 2: "The comfort level is great but if headband is too tight, after 5-6 sets of experiments (about an hour) I could feel a little bit of a headache."

Subject 3: "This is a great probe holder. I have been subject for earlier probe holder too but this is much lighter, comfortable and subject friendly."

2.1.1. The New Probe Holder Stand

(a)   (b)

Figure 2.5: Stand with Probes and without the Probe Holder (a) Front View of the Stand, (b) Side View of the Stand

Figure 2.6: Stand with Probes on the Subject's Head.

The weight of the DYNOT probes has always been an area of concern for the experiments. Due to weight of these probes it was impossible to do 5-6 experiments continuously without the subject feeling pain. To address this problem, after having designed the probe holder we also designed a new probe holder stand to support the weight of each probe individually, so that only a short section of each fiber bundle rests its weight onto the subject's head.

The probe holder consists of the following components (Fig. 2.5(a) and 2.5(b)):

(1) Wooden Base: This base was used in order to counterbalance the weight of the probes.

(2) Fixed Columns: Two fixed columns were mounted onto the heavy wooden base so that it gives support to the whole upper assembly.

(3) Sliding Columns: Sliding columns give the freedom to adjust the height of the stand according to the desired requirements of the experiment.

23

(4) Top Plank: Holes were drilled for individual probes through the top wooden plank thus supporting the weight of each probe, except for the length of the probe extending from the plank to the head's surface.

Limitations of the Experimental Setup

Hardware limitations of the DYNOT system resulted in a maximum number of 32 source-detector pairs being used over a FOV size of 8.4 x 12 cm area spanning the premotor, motor and sensory cortex under the following constraints:

(1) Because we have limited number of source detector pairs, imaging of cortical activation was performed in only one hemisphere.

(2) Due to time multiplexing the signal sampling frequency was limited to 1.81 Hz. This is lowest possible sampling frequency as hemodynamics signals are in the range of 0.1-1 Hz [19].

2.3 fNIRS Activation Protocols

2.3.1. Probe Holder Placement

DYNOT probe placement was done before starting each experiment according to the measured coronal (ear to ear) and sagittal (forehead to back of head) distances. The center of the probe set was placed at half the distance of the aforementioned measurements, which was considered the estimated midpoint of the motor cortex. In a single session 5 protocols were performed including baseline. These totals 5 sessions took overall 25 minutes. For each subject we performed one repeat session for which we tested the reproducibility of cortical activation in the same areas (Exception: Subject 3 had to do sequential tapping thrice as the data acquisition in the second trial was noisy. The reasons may be poor optical contact due to improper placement of the optodes). We estimate the error in probe placement for repeated experiments performed at different days to be ~±2 mm.

2.3.2. Activation Protocols

As the probe holder covers the premotor, motor, and sensory cortex we designed different protocols in order to activate different cortical regions of the brain. In this study, 3 subjects were studied (25 ± 3 years old). The following protocols were performed while subjects were sitting in a comfortable chair in a dimly lit dark room and following directions from a PowerPoint presentation on a PC in front of them. The cues for protocol execution were thus only visual as we avoided eliciting auditory cortex activation. All protocols began with a 30 s baseline where the subject remained inactive and was repeated over 5 epochs.
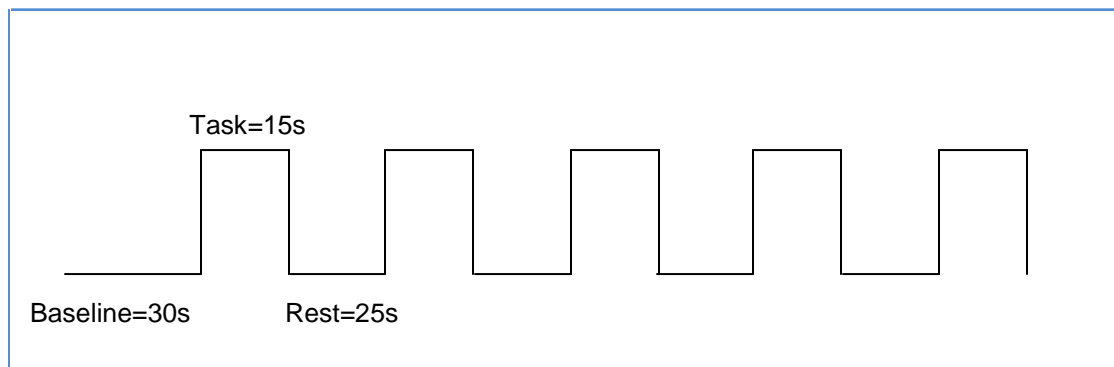
Figure 2.7: Common Protocol Showing Duration of Task, Rest and Baseline

(1) Finger Tip Brushing (FTB): The protocol consisted of 15 s of rubbing a tooth brush (Oral B) on the index finger tip followed by 25 s of rest. This protocol was used as a control for localizing activations in the sensory cortex [53].

(2) Soft Ball Squeezing (Squeeze): The protocol consisted of 15 s of squeezing a sponge ball and 25 s of rest. This was used to find activations in the motor cortex [54].

(3) Finger Tapping (FT): The protocol consisted of 15 s of tapping and 25 s of rest. This protocol intended to measure activations in the motor and sensory cortex [43, 44].

(4) Sequential Finger Tapping (ST): The protocol consisted of 15 s of sequential tapping and 25 s of rest. This protocol was used to find activations in medial premotor, motor and sensory cortex [45].

(5) Card Flipping: This protocol consisted of 30 s of baseline, 15 s of card flipping followed by 25 s of rest. The protocol consisted of 5 epochs. In the experiment we expect to see activation in lateral premotor cortex, motor cortex and sensory cortex

CHAPTER 3

DATA ANALYSIS

The reflectance raw data was obtained from DYNOT machine. The following flowchart describes the overview of the subsequent data analysis.
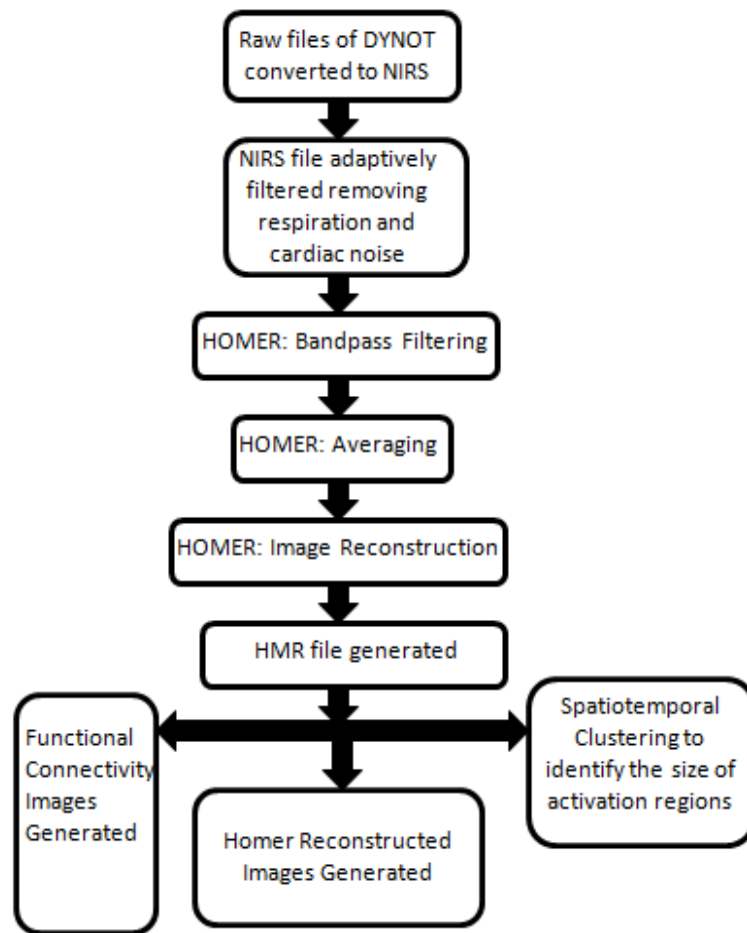
Figure 3.1: Flowchart Showing Overall Data Processing Steps

3.1 Adaptive Filtering

The NIRS file obtained from the DYNOT format conversion code (Courtesy : Fenghua Tian) may contain many noise artifacts that could lead to corrupted activation images if not filtered properly.   These sources of noise originate from physiological hemodynamics and consist of cardiac pulsation, respiration and Mayer waves (refs) Adaptive filtering can remove the contribution of these superficial hemodynamics from the detected activation signal even though the latter may overlap with the frequency range of the signal [38].   In the adaptive filtering algorithm a baseline correction was done first for each activation block.   Optodes 13 and 17 were used as physiological noise references for adaptive filtering as these were at the two opposite edges of the FOV to that spatial variations of superficial hemodynamics could better assessed.   The physical separation of optodes 13 and 17 with the nearest detector was 1.1 cm so that the back-reflected light would mostly sample superficial hemodynamics.   We have used the signal from optode 17 as the adaptive filter reference for the top half of the optodes and 13 for the bottom half.
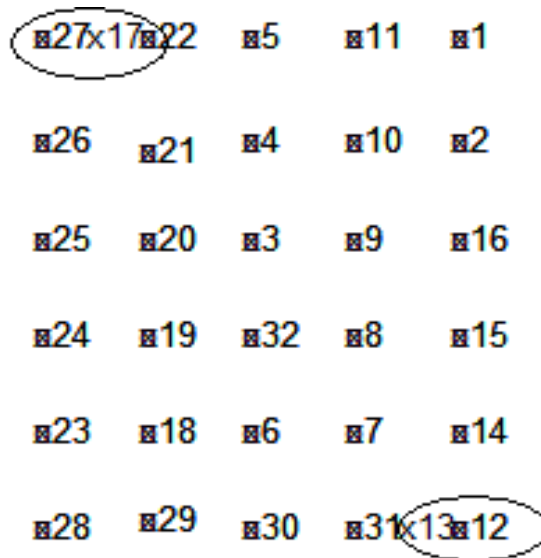
Figure 3.2: Channels used for Adaptive filtering
(Source 13- Detector 12, Source 17- Detector 27)

3.2 HomER

HomER stands for "Hemodynamic Evoked Response". HomER is a MATLAB based graphical user interface program, developed to facilitate the processing of optical functional brain data. It analyzes functional near infrared data and has tools for filtering, data averaging, linear regression, and 2D image reconstruction.   HomER gives the user full control of the measurement configuration and probe properties [39].

After a NIRS file was adaptively filtered we used the following three main HomER steps for further data processing:

3.2.1 Filtering

Filtering consists of a number of calculations including low and high pass filtering of the data which are user-defined for use we used 0.01 to 0.3 Hz and principle component analysis filtering. PCA is used to remove systemic fluctuations present in NIRS data. The band pass filter removes cardiac or slow drifts. The PCA can partially remove global artifacts like breathing or Meyer waves, which contain frequencies the 0.1-0.3 Hz range. We used band pass filter then used PCA filtering during data analysis.
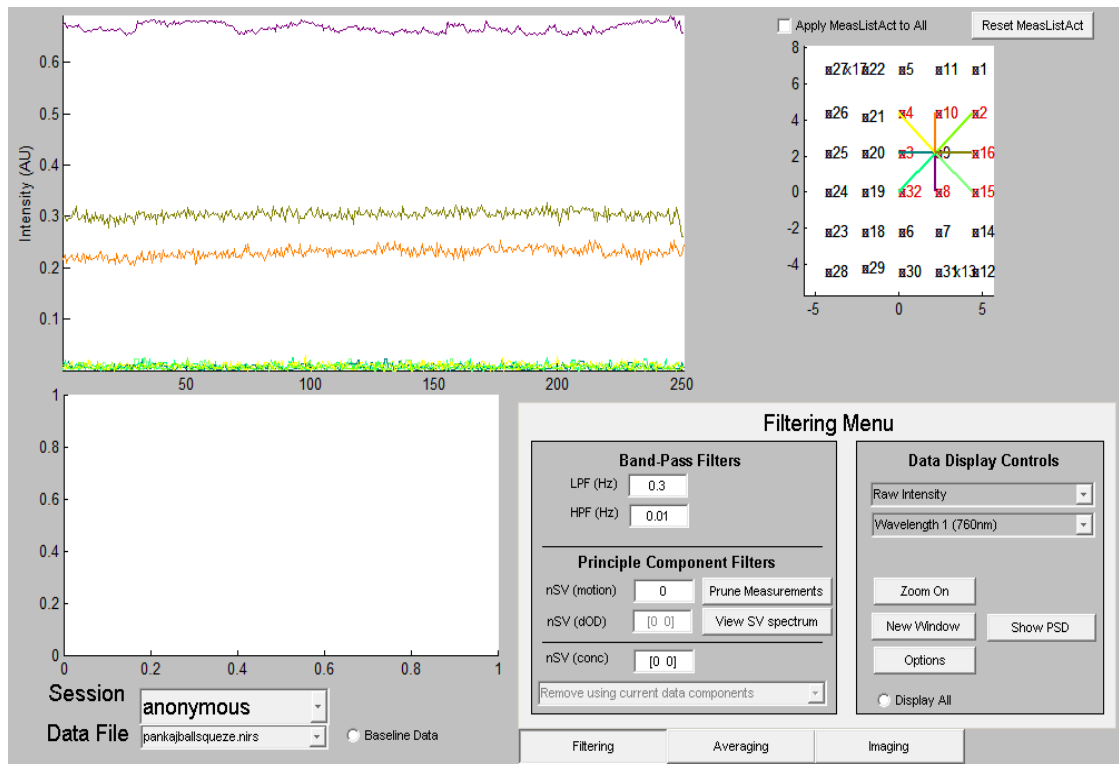
Figure 3.3: Sample of the HomER Filtering GUI

3.2.2 Averaging

This section of HomER is used to analyze functional hemodynamic responses in which we can define the time averaging window relative to the stimulus duration. HomER supports both block-designed and event-related paradigms. The localization of activation can be done through a GUI that enables the display of hemodynamic response data for individual source-detector pairs. At first we define the stimulus duration window by marking in the GUI the time points relevant to the execution of the protocol: 30 s of baseline and 40 s of each block (15 s or body activity + 25 s of rest) for 5 blocks. The total duration of the experiment was 210 s, i.e. three and a half minutes. Then we defined the time averaging window for the block-averaged

data with a pre-stimulus duration of 5 s (i.e. five seconds before a new block begins) and post-stimulus as 40 s.
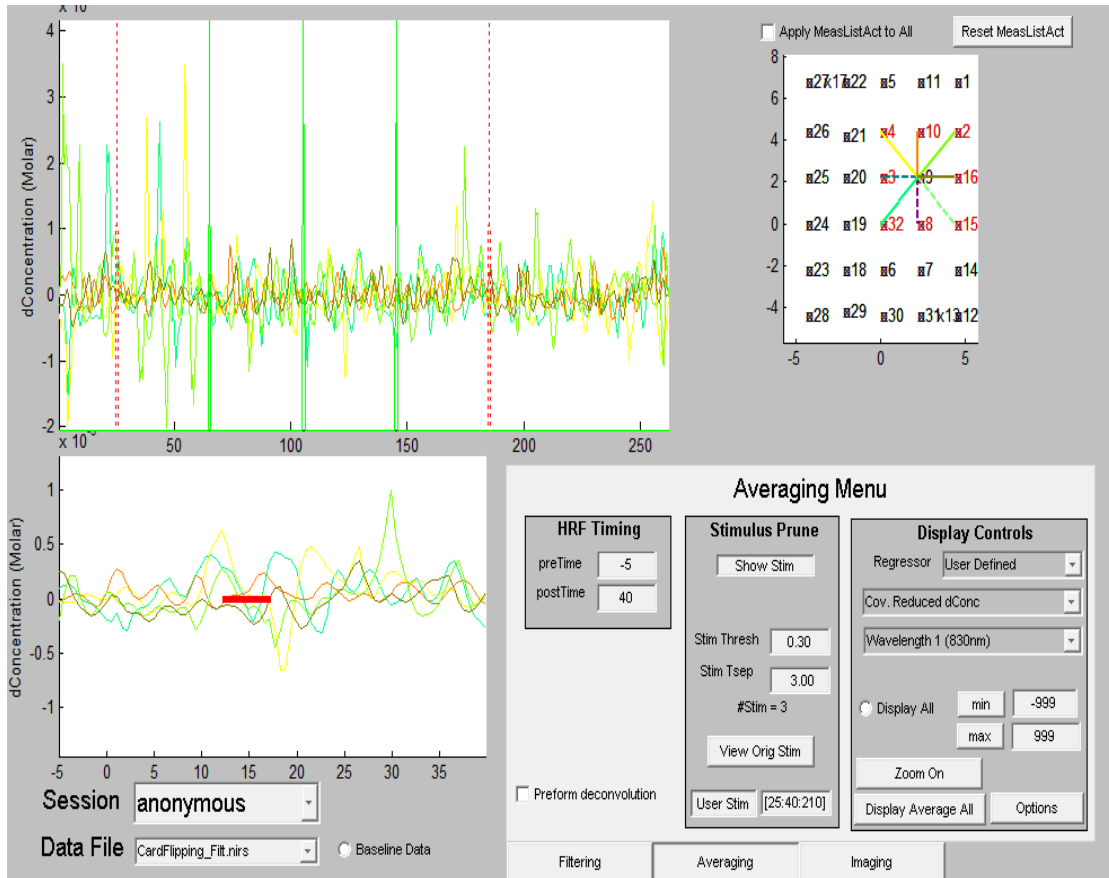
Figure 3.4: Averaging Section of HomER

3.2.3 Image Reconstruction

HomER has two options for image reconstruction, namely backprojection and a Moore-Penrose regularized inversion. For this work the Moore-Penrose regularized inversion was used to yield fNIRS images [55]. The image reconstruction can be done for DOD (optical density) or for Hb and HbO concentration changes. We used the second option. The background absorption and scattering coefficients used in this work were 0.05 cm^{-1} for

absorption and 10.00 cm^{-1} for reduced scattering and a voxel size of 8.80 x 11.2 x 1 mm was used.
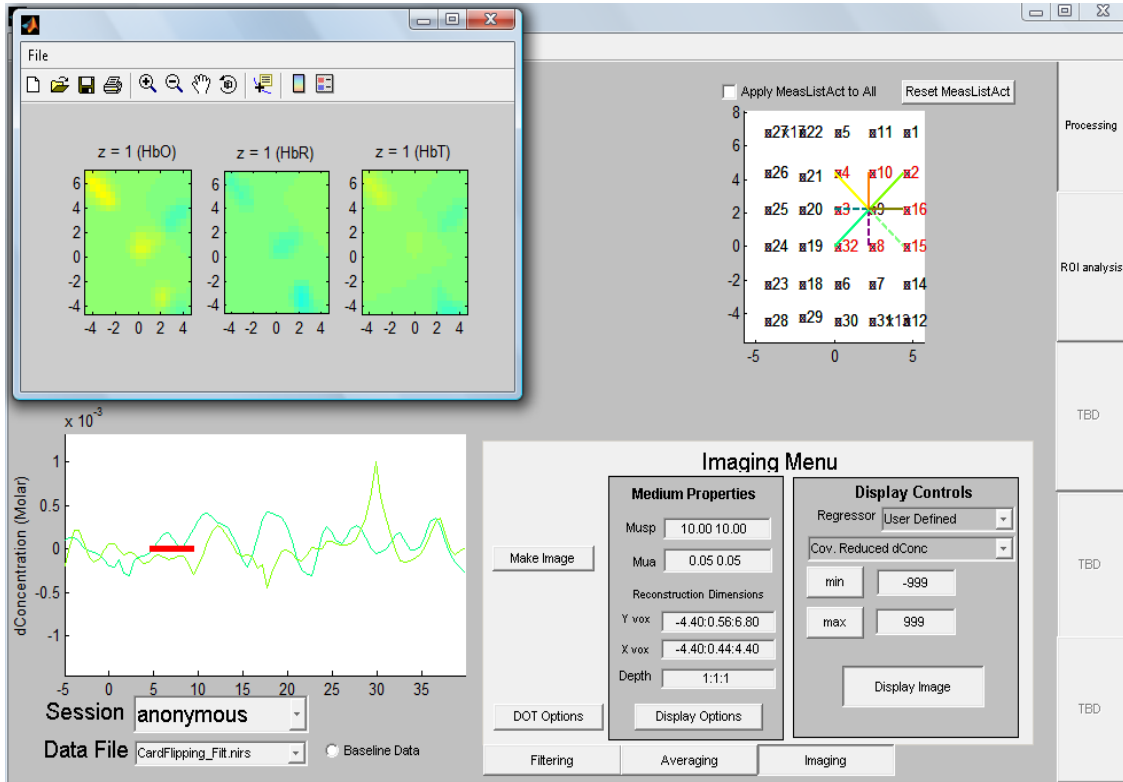
Figure 3.5: Snapshot of Image Reconstruction GUI in HomER.

3.3 Spatiotemporal clustering

When reconstructed images are displayed in HomER one can usually see hot spots of activation or deactivation that are denoted by red and blue colors respectively. These hot spots are separated by areas of green that is the color code for little or no activation with respect to baseline values. In this setting the apparent size of activation/deactivation areas is rather subjective as it depends on the color scale used to display the image. Here we present the application of a spatiotemporal clustering algorithm that groups pixels in areas of similar activation patterns, i.e. the same number of troughs, peaks and zero nodes in their activation

31

time-series, irrespective of peak and trough amplitude. In this fashion, pixels with similar activation time-series patterns are grouped in the same cluster irrespective of whether the total activation amplitude is strong or weak. This approach provides a quantitative means of assessing whether a pixel is associated with a given activation pattern, which is information that is not evident from visual inspection of activation images.
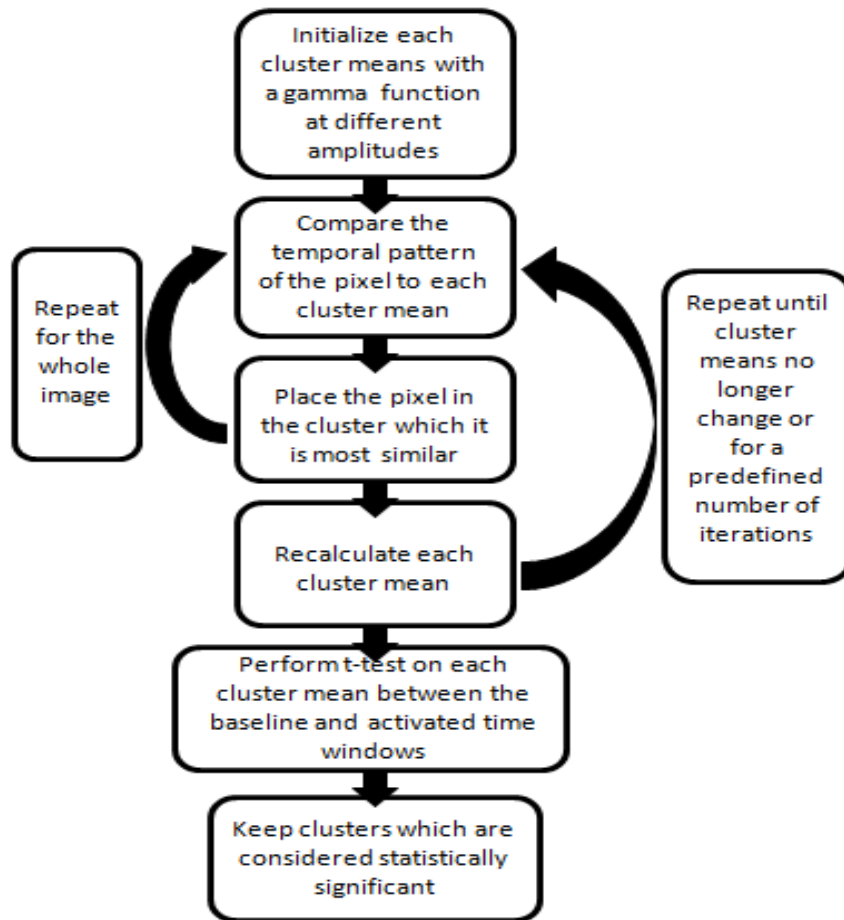
Figure 3.6: Flow Chart for Spatiotemporal Clustering Algorithm

The flowchart for the spatiotemporal clustering algorithm is shown in Figure 3.4. The spatiotemporal clustering algorithm begins by initializing each cluster mean by a gamma function at different amplitudes convolved with the duration of activation specified in the

protocol. This initialization action simulates the typical shape of an activation stimulus, as the initial range of values belonging to each cluster. The range of amplitudes initially assigned to each cluster was determined by the number of clusters, i.e. (max pixel value – min pixel value)/(number of clusters). Subsequently pixels were reassigned clusters by comparing their temporal pattern to the current cluster mean. The pixels were assigned to clusters for which their activation time series was most similar to the current mean cluster time-series waveform. The similarity metric with which this comparison was performed was a combination of both the Euclidean distance and the correlation coefficient. This procedure was repeated for the time-series data of each pixel in the image. The cluster means were then recalculated and a t-test was performed to decide if certain clusters were identical and needed to be merged. This whole process was repeated until the cluster means no longer changed, or until a predefined number of iterations (400) were met [40]. It was empirically found that no more than 15 clusters need to be used in this algorithm, as larger initial numbers of clusters were merged by this algorithm to a number that was always less than 15 for all the analyses performed in this work.
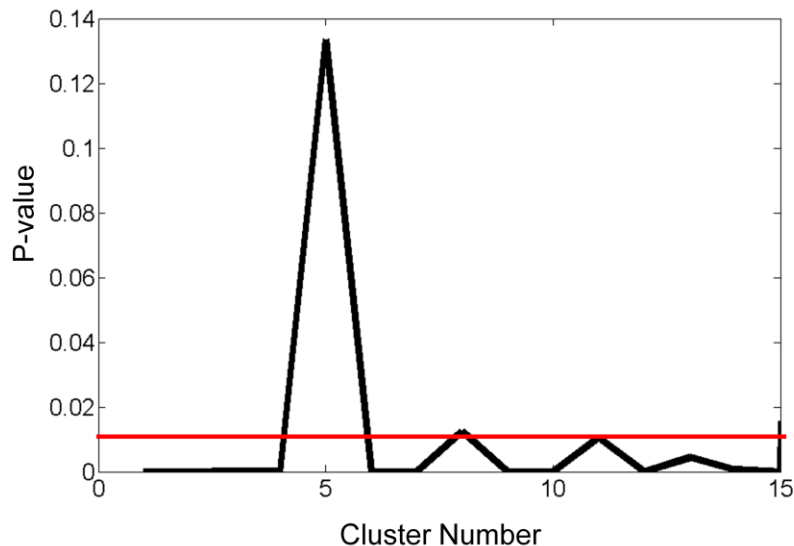
Figure 3.7: Example of how a P-Value of 0.01 Results in the Identification of a Cluster as Activation/Deactivation

33

Once the image was clustered a t-test was performed on the cluster means between the baseline time window and a similar time window during activation to determine if the cluster had significant activation (Figure 3.5). A baseline p-value of 0.1 was assumed to be the threshold for deciding which clusters belonged to activation/deactivation and not baseline. The algorithm considered absolute amplitudes only, so activation (positive HbO change) was differentiated from deactivation (negative HbO change) by comparing with the original activation images.
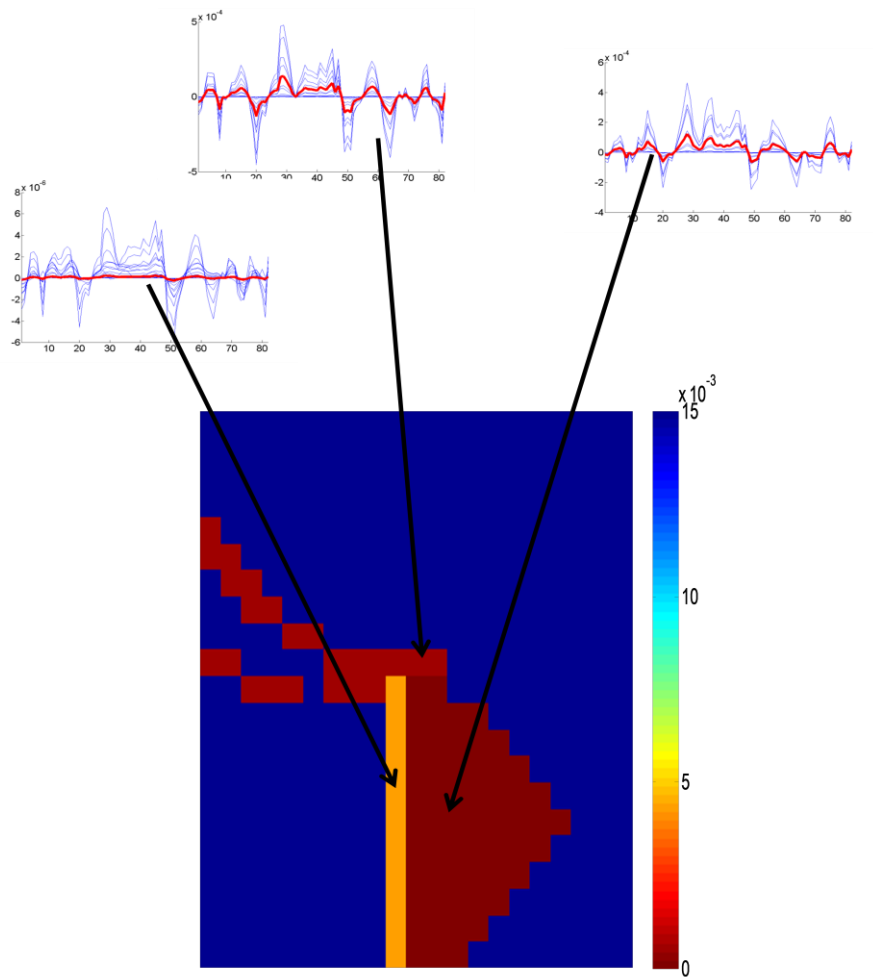
Figure 3.8: Reconstructed Image based on chosen P value

Figure 3.6 shows an example of a clustered image with the arrows indicating the range of spatiotemporal patterns grouped in each cluster during a brsuh protocol. A p-value of 0.1 was selected which is considered as a widely used p-value in statistical analysis, which resulted in an image only showing only 5 clusters with significant activation. The color scale on the right side simply indicates clusters according to their p-value.

3.4 Functional Connectivity

Cerebral hemodynamic fluctuations or spontaneous fluctuations in brain are characterized by their low frequency (< 0.1 Hz), can occur even in the absence of a task, and are often correlated between functionally related areas. Although the origin is still uncertain, it has been hypothesized that correlated fluctuations reflect synchronized variations in the neuronal activity of brain areas, and are characteristic of functional connections among different networks of the brain. The assumption that the origin of such correlated fluctuations is neuronal is supported by observed coherent ongoing activity in neuronal discharge patterns. Clinical studies have demonstrated that resting-state connectivity is altered in disorders such as stroke, Alzheimer's disease, schizophrenia, multiple sclerosis, autism and epilepsy, suggesting a disruption of neuronal and/or vascular factors that contribute to high correlation in these networks [56].

Functional connectivity is defined as the correlation of low frequency fluctuations in brain, which may arise from fluctuations in blood oxygenation or flow, is a manifestation of functional connectivity of the brain [57].

To find any functional connection between promoter, motor and sensory cortex locations during the resting state the functional connectivity (normalized cross-correlation) was computed between seed pixels in each one of these regions and the rest of the pixels in the FOV. The seed pixels were chosen as the ones having the maximum positive ΔHbO value in

35

the activation image created by a protocol eliciting activation in that region.   More specifically the seed pixel for the sensory cortex was selected from the brush protocol, the motor cortex seed pixel from the soft ball squeeze protocol, and the premotor cortex seed from the sequential tapping protocol [41].

CHAPTER 4

RESULTS AND DISCUSSION

In order to study activation patterns in the premotor, motor and sensory cortices, fNIRS protocols for sensory and motor tasks involving the dominant hand of three able bodied subjects were performed while the optodes were placed over the contralateral hemisphere of activation. More specifically, with the optodes placed over the premotor and sensorymotor cortex, subjects performed the following sensory and motor tasks: brushing of the forefinger, squeezing a soft ball, finger tapping and sequential finger tapping, all with the right hand. The tasks were designed to activate different parts of the cortex pertaining to sensory and motor stimuli and individual subject measurements were recorded and processed.

Fig. 4.1(a) shows the activation time sequence, averaged in five second intervals, as elicited when the brush protocol was applied to Subject 1. The subject was immobile and when tactile input was given by another attending participant strong localized activation was seen in the sensory cortex. These experiments functioned as controls for localizing the sensory cortex. In the squeeze protocol the subject was given a soft ball and was instructed to squeeze according to the protocol described previously. During squeeze, since subjects ware using many of their hand muscles hands strong activation was observed in the motor cortex area. The intensity of this repetitive motion was most likely responsible for the early rise of activation that was seen within the first 5 s window, which persisted almost for the entire duration of the epoch, out to 30 s. The squeeze protocol was primarily designed for localizing the motor cortex in the FOV.

Figure 4.1(c) shows the activation pattern resulting from the subject performing finger tapping.   In this protocol the activation resulting from tapping in the 0-15 s window was primarily seen in motor cortex and within the 5-20 s window and took 15-20 s to attain its peak, which was longer compared to the squeeze protocol.   This delay in peak time could be attributed to the weaker levels of muscular activity that the finger tapping task entails.

 Sequential tapping was designed in order to elicit activations in premotor, motor and sensory cortices as it would involve the subject's cognitive, i.e. planning of the motion in the premotor area, and sensorimotor cortical circuits [45].   The activations obtained were indeed located in the subject's premotor motor and sensory areas, but the intensity of activation for the motor region was weak, most likely due to the very low speed with which this task was performed,i.e this task entailed lower muscular activity than finger tapping in tandem with all fingers.

The activations obtained were indeed located in the subject's premotor motor and sensory areas, but the intensity of activation for the motor region was weaker, most likely due to the very low speed with which this task was performed, .i.e. this task entailed lower muscular activity than finger tapping in tandem with all fingers.

38
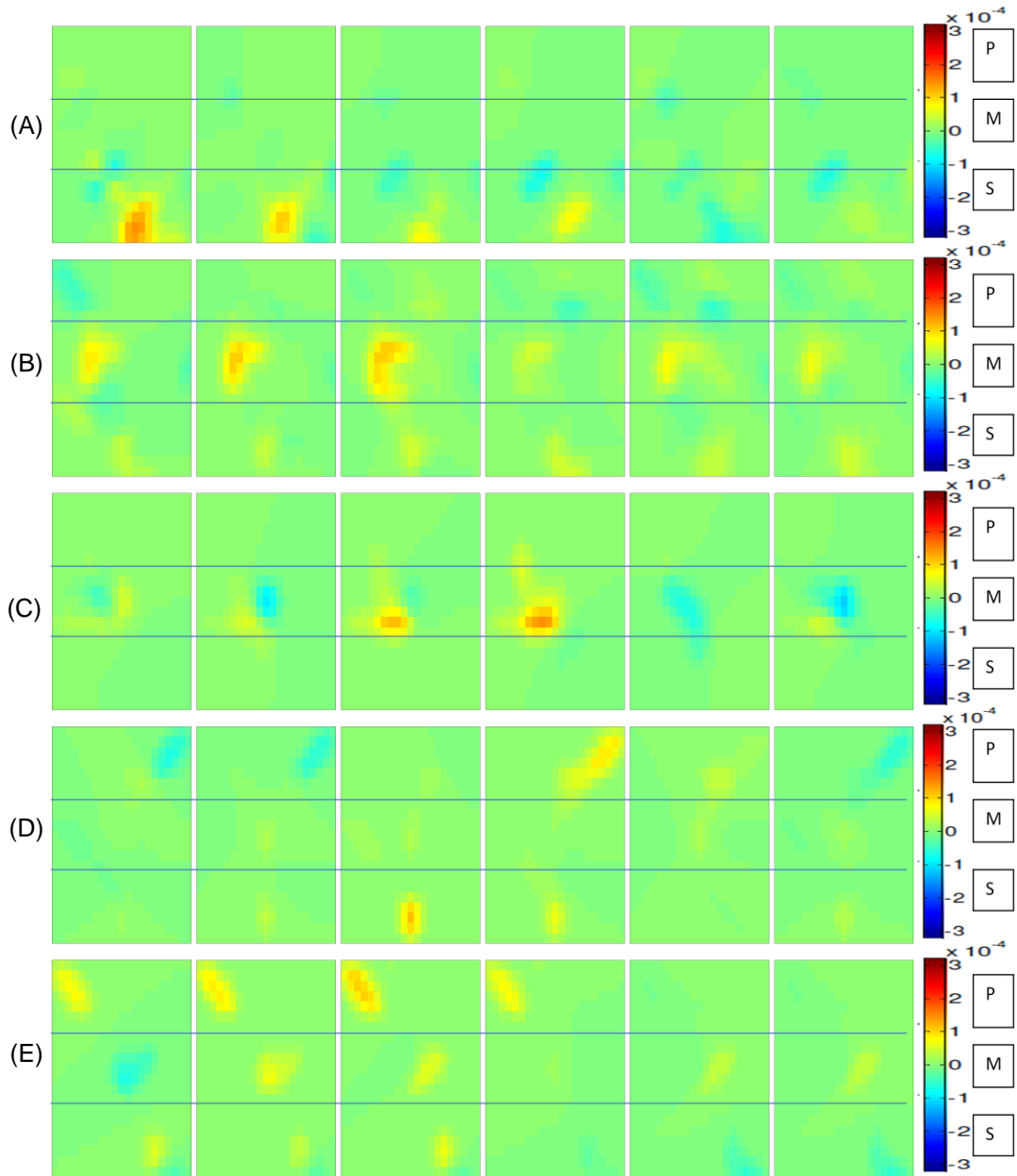
Figure 4.1: Figure shows various protocols used in the experiment with duration 5s from 0-30s and activations obtained in various cortices (A) Brush Protocol, (B) Squeeze Protocol, (C) Tap Protocol, (D) Sequential Tap Protocol, (E) Card Flipping Protocol.

In order to validate our results we performed all five sets of experiments on three different subjects as shown in averaged reconstruction images given below in Figure 4.2. The epoch length for squeeze was 45 s and the length was determined after trial and error for different lengt of intervals between epochs.
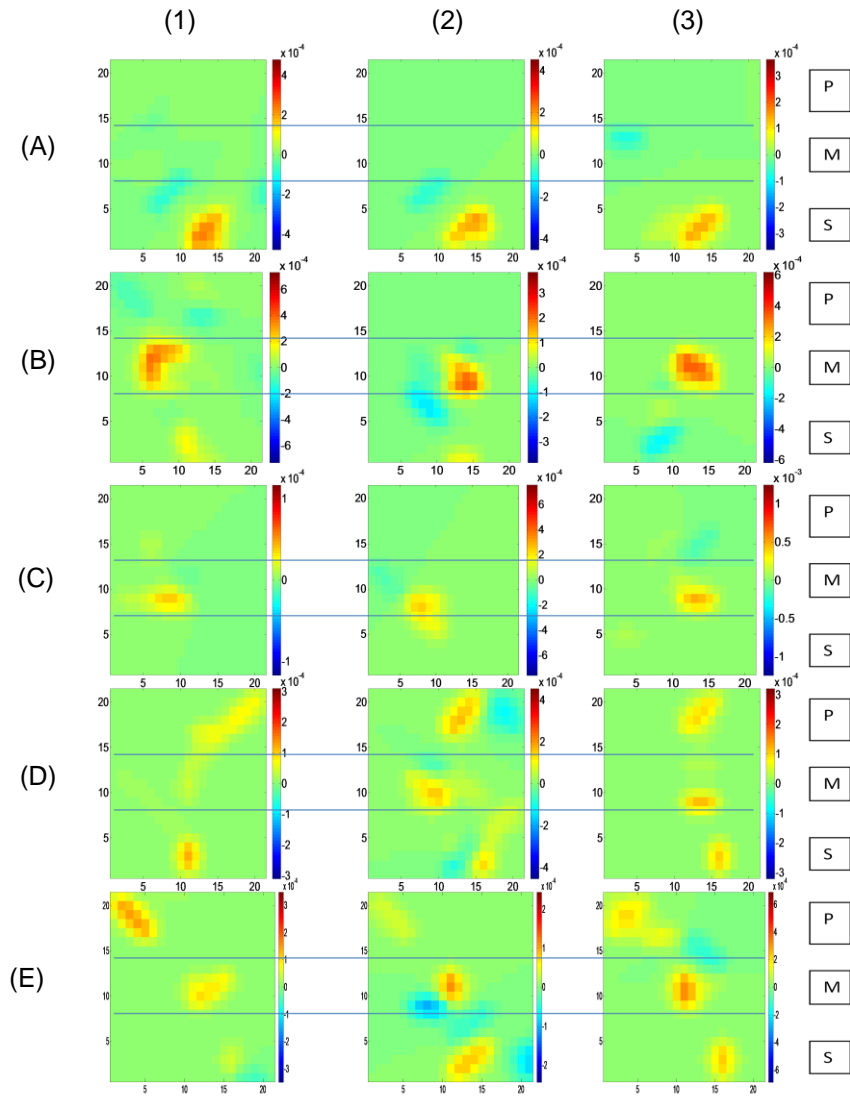
Figure 4.2: Time-Averaged Reconstruction Images (5-20 s) for Three Subjects Each Performing Indicated Protocols (A –E) with Corresponding Activation Patterns in Different Cortices of Brain (A) Brush Protocol, (B) Squeeze Protocol, (C) Tap Protocol, (D) Sequential Tap Protocol, (E) Card Flipping Protocol. (1) Subject 1, (2) Subject 2, (3) Subject 3

Figure 4.2 shows the time-averaged activation (5-25 s) for each of the three subjects performing each protocol: finger tip brushing, squeezing, finger tapping and sequential finger tapping. Each subject performed all these protocols in a single session so that source-detector positions did not vary between protocols.

For the brush protocol we found similar activation patterns in the sensory cortex for all the subjects. This result can be attributed to the fact that the subject's hand was immobile and the tactile stimuli elicited by the brush were given by other person in order to minimize any muscle movements by the subject during the task. This protocol gives the localization of the sensory cortex in the reconstructed activation images.

In the squeeze protocol as depicted in Figure 4.2(b) we found strong activation in the motor cortex region when the subjects were asked to squeeze the soft ball according to the protocol. The stronger activation can be attributed to the high intensity of the movement and the fact that many hand muscles participate in this process leading to an increased regional cerebral blood flow in the motor cortex. In all three subjects similar activation patterns were found giving localization of the motor cortex in the reconstructed images though some sensory activation was also seen.

The finger tapping protocol is considered the conventional method to study motor cortex activation.   Activations resulting from this protocol are depicted in Figure 4.2(c). Activation was indeed only discernible in the motor cortex region at edge of the border with the sensory area. As the finger tapping activity required less muscle activity than the squeezing a somewhat less intense and smaller apparent activation area was seen for this protocol. The frequency of tapping was 1 Hz whereas the frequency of squeeze was 0.8 Hz.

In the sequential finger tapping protocol as depicted in Figure 4.2(d) activations were found in the medial premotor, motor and sensory cortices of the left hemisphere for all the three

41

subjects. The sequential tapping elicits activation in some of the same regions activated by the squeeze and brush protocols, but in addition it elicits activation in the medial premotor region.

In the card flipping protocol activations were found in the lateral premotor, motor and sensory cortices of the left hemisphere for all the three subjects. The activations in the motor and sensory regions had the same localization as the ones found for the case of the brush and squeeze protocols. However, this protocol helps localize the lateral premotor cortex.
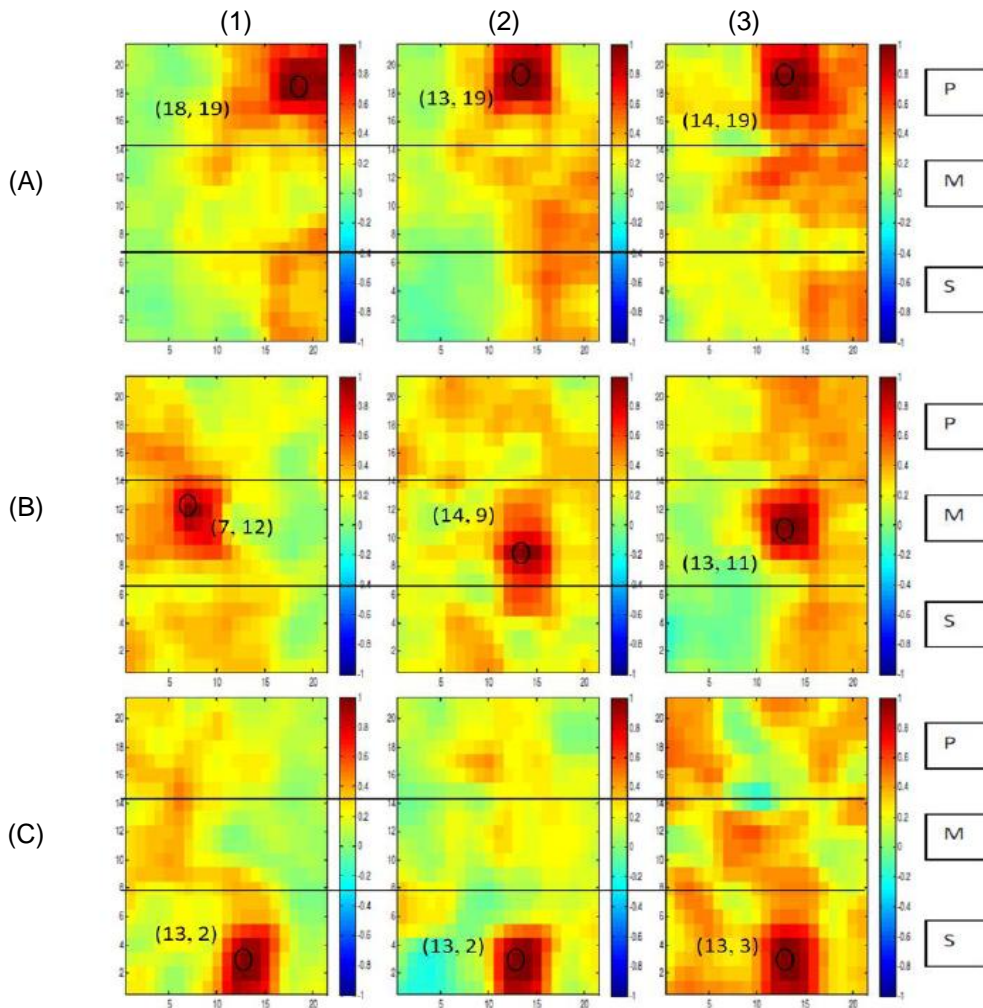
Figure 4.3: Functional Connectivity Depicting Resting State Connectivity between Premotor, Motor and Sensory Cortices for all Three subjects (1) Subject 1, (2) Subject 2, (3) Subject 3 (A) Premotor Cortex, (B) Motor Cortex, (C) Sensory Cortex

Figure 4.3 depicts the spatiotemporal correlations over the premotor, motor and sensory cortex for all the three subjects during the resting state [54]. By choosing the pixel with maximum activation for each of the premotor, motor and sensory areas of each subject as seeds, we computed the normalized cross-correlation between each of the seed pixels and every other pixel in the image. In the figure, the chosen seed location is depicted as an oval and its position is indicated in brackets.

As illustrated in Figure 4.3(a) for Subject 1 we have chosen maximum activity locations during prior activation protocols as seeds for computing the resting state connectivity in the premotor, motor and sensory cortices. We see all the three regions are functionally correlated in a robust way. Interestingly, when the seed was taken in the premotor cortex correlations beyond the premotor cortex were found to be stronger with the sensory than with the motor cortex. This phenomenon was seen twice when experiments were repeated on separate days. When the seed pixel was taken in the motor cortex it was seen that the motor is correlated to the premotor and sensory cortex almost equally. Furthermore, for the sensory cortex seed we observed almost equal spatiotemporal correlations with the premotor and motor regions.

For Subject 2 we chose the maximum activated pixels in premotor, motor and sensory cortices as depicted in Fig. 4.4. From the figure it can be observed that for each of the sensory and motor seed pixels, the spatiotemporal correlation was equally robust with the other two cortical regions. Furthermore, for the sensory cortex we observed that resting state connectivity was equally strong with the premotor and motor cortex though the patterns were different from those of Subject 1. The experiment done on same subject on a separate day revealed a similar correlation pattern.

Similarly, for Subject 3 seed pixels were chosen in three cortical regions as shown in Figure 4.3(c). For each of the premotor, motor and sensory regions, we observed that all seed

43

pixels had strong correlation with all other regions. When the experiment was repeated on a second day, the data for this subject were very noisy due to bad optical contact.

Fig 4.4 shows the baseline data for all three subjects which shows the hemodynamic fluctuations in the brain during resting state.
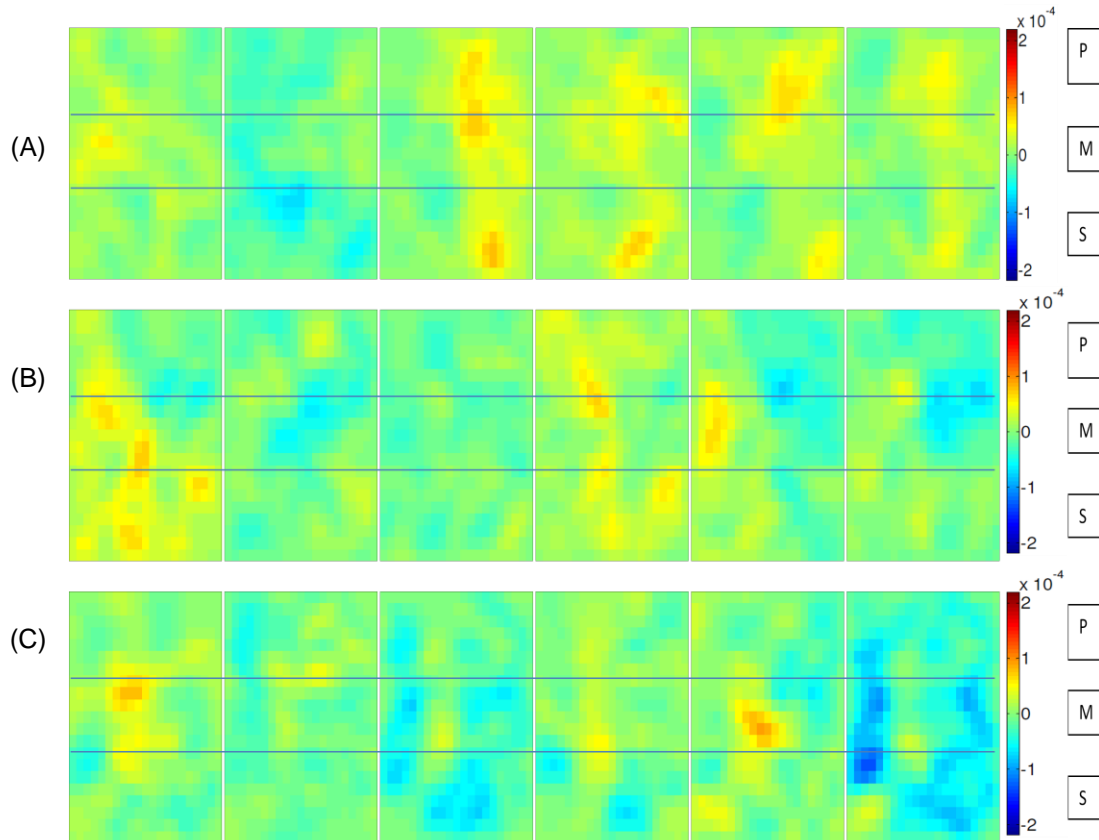
Figure 4.4: Baseline Data for All Three Subjects with the duration of 5s from 0-30s
(A) Subject 1, (B) Subject 2, (C) Subject 3
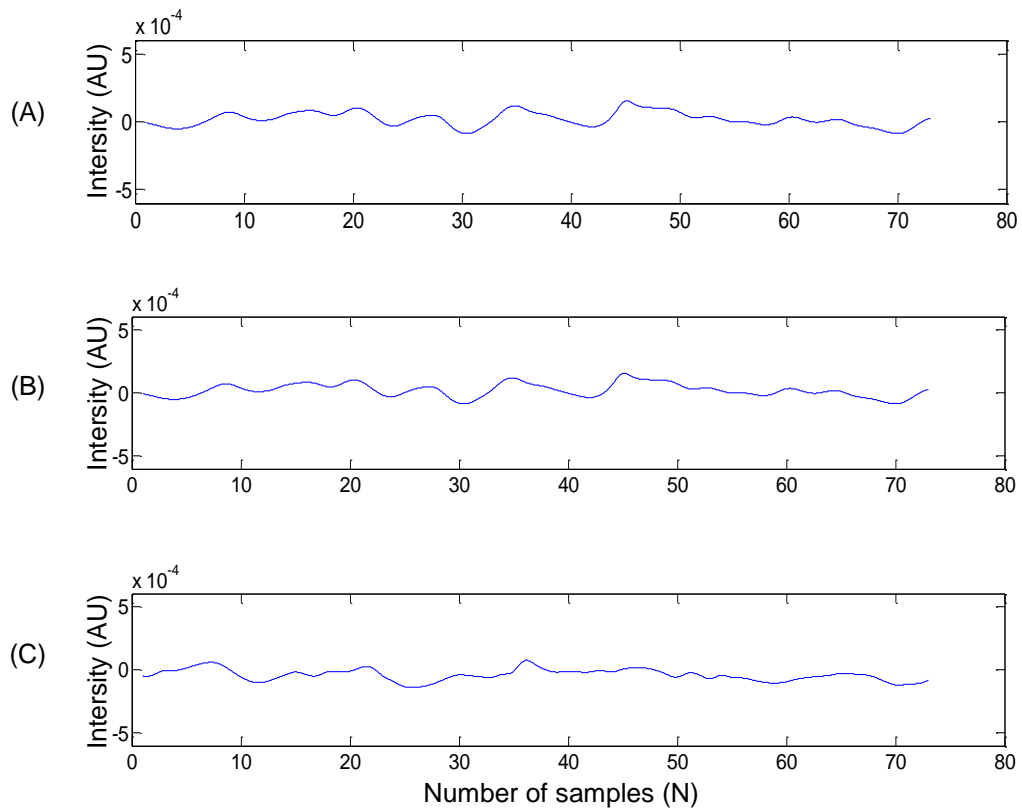
Figure 4.5: Baseline data Signal for All Three Subjects
(A) Subject 1, (B) Subject 2, (C) Subject 3

Above figure 4.5 shows baseline signal for all three subjects showing lower frequency hemodynamic fluctuations in the brain. The signal intensity for activation and deactivation patterns is very low.

Fig. 4.4 below depicts results from the spatiotemporal algorithm that clusters cortical regions with similar activation patterns for all the three subjects.
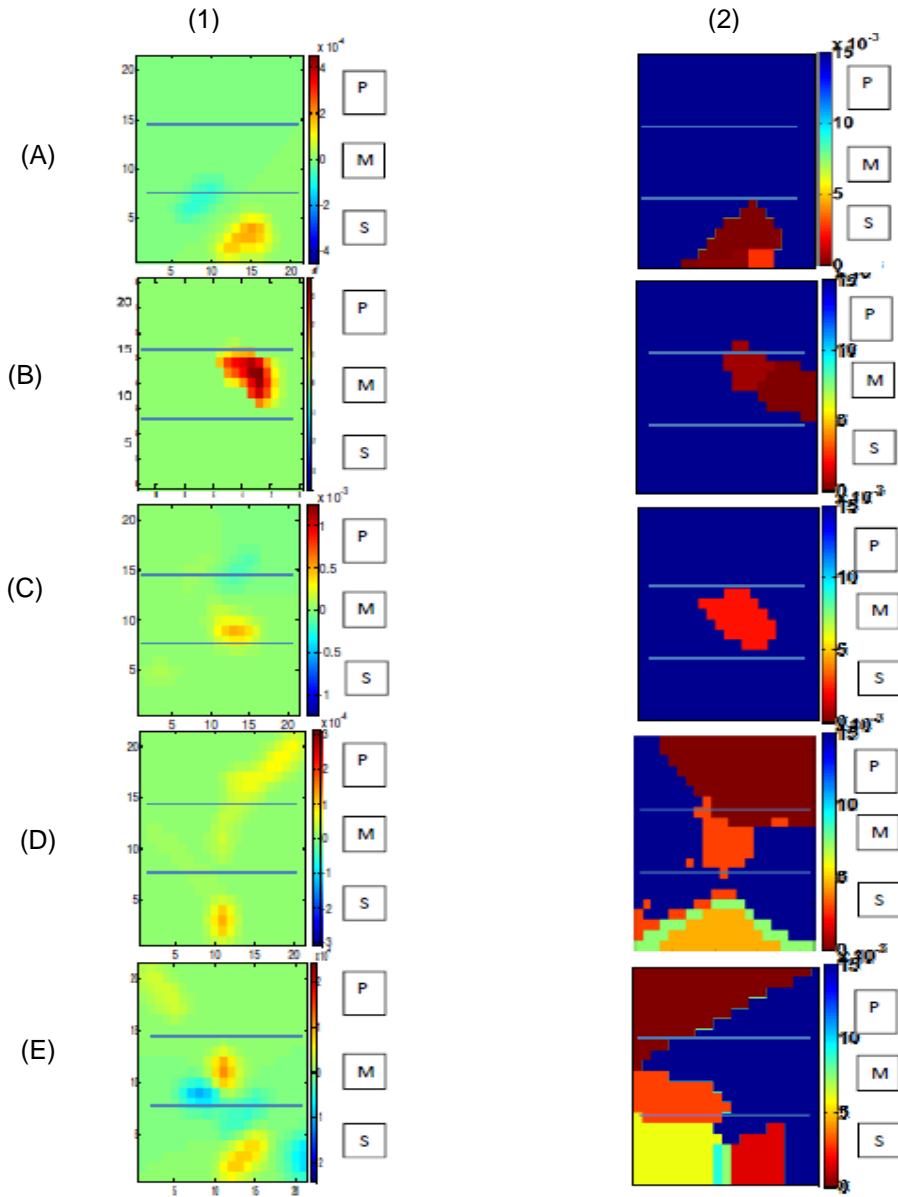
Figure 4.6: Spatiotemporal Cluster Images for all Three Subjects Shown against the Corresponding Activation Images. (A) Brush Protocol, (B) Squeeze Protocol, (C) Tap Protocol, (D) Sequential Tap Protocol, (E) Card Flipping Protocol, (1) Average Reconstruction Images, (2) Spatiotemporal Images.

For the brush protocol, we see predominantly weaker activations in the sensory cortex for all the three subjects. In addition we also see some weak activation in motor cortex that are not visible in original reconstruction images.

For squeeze protocol, muscular involvement is greater thereby contributing to a rapid increase in brain perfusion and this gives rise to weaker activations in all the three cortices for all subjects except Subject 2. The reason for exception in Subject 2 may be due to the fact that subject was applying less force in squeezing as compared to other subjects resulting in a lesser degree of cerebral blood flow rise.

For the tapping protocol, we get activations in motor and sensory areas for all the three subjects. As no cognitive task was involved in this protocol we didn't see any activation in premotor areas.

In sequential tapping, which is expected to activate centers in all three regions, we indeed get activations in all the three cortical regions for all the three subjects.

The threshold image obtained from the spatiotemporal images is determined by the p values chosen (0.01 or 0.05), as described in Figure 4.4 above.

CHAPTER 5

CONCLUSION AND FUTURE WORK

In this work we have made a probe holder assembly that enables wider FOV) imaging of cortical regions with the DYNOT system than was previously possible. Prior studies with a more restricted FOV required moving the probe assembly to different regions depending on where activation was to be recorded. In the present assembly system activation can be recorded in the entire premotor, motor and sensory area of one brain hemisphere. We have implemented a series of protocols that elicits activations in each of these cortical regions and have studied the differences between protocols in the resulting spatiotemporal patterns. These differences were studied (a) by visual inspection of the activation regions in reconstructed images, (b) resting state connectivity between these regions, and (c) the clustering of different regions according to similarities in their spatiotemporal activation patterns.

The probe holder mask designed and constructed by us is light weight, comfortable and easy to wear as compared to the conventional DYNOT probe holder. In addition, a probe holder stand was specially designed so as to support the individual weights of the probes. This stand proved quite useful is supporting a lot of the fiber bundle probe weight so that only a very short overhanging portion of those fibers, i.e. the fiber bundle length between the supporting shelf and the subject's head, is the one being supported by the subject's head.

Though we designed the above two research tools to enable more effective use of the DYNOT system, still dark dense hair in one of the subjects created a major problem. Hair needs to be displaced from under the sources and detectors, and when positioning the probe on the head, we did our best to optimize the coupling of all fiber tips. However, given the physical

48

size of these fiber bundles it is impossible to eliminate all the hair from underneath the probe surface, especially for subjects with thick hair.

In the future, work can be done over a larger cortical area if more source-detector pairs can become available on the DYMOT system, or in fact on any other fNIRS system such as the CW-6 or the Cephalogics ones. The limitation is seen to be financial rather than coming from supporting the weight of the fiber bundles In addition, using an imaging system like the CW6 or the Ceplhalogics system will offer higher sampling rate, which may in turn enable improved discrimination in time of response between different cortical regions. Lastly, outfitting the fiber bundle probes with brush optodes will potentially improve optical contact, especially for subjects with thick hair, will shorten setup time and will make the overall fNIRS experience more subject-friendly.

APPENDIX A

DYNOT MATLAB CONVERSION CODE

```
close all;
clear all;
clc;

fid = 'NIRS File';

%TODO #1:
%Specify the wavelengths
SD.Lambda=[830 760];

%TODO #2:
%Specify Source Positions [X Y Z] in centimeters
SD.SrcPos(1,:)  = [ 4.4   6.8   0];
SD.SrcPos(2,:)  = [ 4.4   4.4   0];
SD.SrcPos(3,:)  = [ 0.0   2.2   0];
SD.SrcPos(4,:)  = [ 0.0   4.4   0];
SD.SrcPos(5,:)  = [ 0.0   6.8   0];
SD.SrcPos(6,:)  = [ 0.0  -2.2   0];
SD.SrcPos(7,:)  = [ 2.2  -2.2   0];
SD.SrcPos(8,:)  = [ 2.2   0.0   0];
SD.SrcPos(9,:)  = [ 2.2   2.2   0];
SD.SrcPos(10,:) = [ 2.2   4.4   0];
SD.SrcPos(11,:) = [ 2.2   6.8   0];
SD.SrcPos(12,:) = [ 4.4  -4.4   0];
SD.SrcPos(13,:) = [ 3.3  -4.4   0];
SD.SrcPos(14,:) = [ 4.4  -2.2   0];
SD.SrcPos(15,:) = [ 4.4   0.0   0];
SD.SrcPos(16,:) = [ 4.4   2.2   0];
SD.SrcPos(17,:) = [-3.3   6.8   0];
SD.SrcPos(18,:) = [-2.2  -2.2   0];
SD.SrcPos(19,:) = [-2.2   0.0   0];
SD.SrcPos(20,:) = [-2.2   2.2   0];
SD.SrcPos(21,:) = [-2.2   4.2   0];
SD.SrcPos(22,:) = [-2.2   6.8   0];
SD.SrcPos(23,:) = [-4.4  -2.2   0];
SD.SrcPos(24,:) = [-4.4   0.0   0];
SD.SrcPos(25,:) = [-4.4   2.2   0];
SD.SrcPos(26,:) = [-4.4   4.4   0];
SD.SrcPos(27,:) = [-4.4   6.8   0];
SD.SrcPos(28,:) = [-4.4  -4.4   0];
SD.SrcPos(29,:) = [-2.2  -4.2   0];
SD.SrcPos(30,:) = [ 0.0  -4.4   0];
SD.SrcPos(31,:) = [ 2.2  -4.4   0];
SD.SrcPos(32,:) = [ 0.0   0.0   0];

SD.DetPos(1,:)  = [ 4.4   6.8   0];
SD.DetPos(2,:)  = [ 4.4   4.4   0];
SD.DetPos(3,:)  = [ 0.0   2.2   0];
SD.DetPos(4,:)  = [ 0.0   4.4   0];
SD.DetPos(5,:)  = [ 0.0   6.8   0];
```

50

```
SD.DetPos(6,:)  = [ 0.0  -2.2   0];
SD.DetPos(7,:)  = [ 2.2  -2.2   0];
SD.DetPos(8,:)  = [ 2.2   0.0   0];
SD.DetPos(9,:)  = [ 2.2   2.2   0];
SD.DetPos(10,:) = [ 2.2   4.4   0];
SD.DetPos(11,:) = [ 2.2   6.8   0];
SD.DetPos(12,:) = [ 4.4  -4.4   0];
SD.DetPos(13,:) = [ 3.3  -4.4   0];
SD.DetPos(14,:) = [ 4.4  -2.2   0];
SD.DetPos(15,:) = [ 4.4   0.0   0];
SD.DetPos(16,:) = [ 4.4   2.2   0];
SD.DetPos(17,:) = [-3.3   6.8   0];
SD.DetPos(18,:) = [-2.2  -2.2   0];
SD.DetPos(19,:) = [-2.2   0.0   0];
SD.DetPos(20,:) = [-2.2   2.2   0];
SD.DetPos(21,:) = [-2.2   4.2   0];
SD.DetPos(22,:) = [-2.2   6.8   0];
SD.DetPos(23,:) = [-4.4  -2.2   0];
SD.DetPos(24,:) = [-4.4   0.0   0];
SD.DetPos(25,:) = [-4.4   2.2   0];
SD.DetPos(26,:) = [-4.4   4.4   0];
SD.DetPos(27,:) = [-4.4   6.8   0];
SD.DetPos(28,:) = [-4.4  -4.4   0];
SD.DetPos(29,:) = [-2.2  -4.2   0];
SD.DetPos(30,:) = [ 0.0  -4.4   0];
SD.DetPos(31,:) = [ 2.2  -4.4   0];
SD.DetPos(32,:) = [ 0.0   0.0   0];

%TODO #3:
%Detector Positions [X Y Z] in centimeters
% SD.DetPos(1,:)  = [ 4.5   2.0   0];
% SD.DetPos(2,:)  = [ 4.5   0.0   0];
% SD.DetPos(3,:)  = [ 4.5  -2.0   0];
% SD.DetPos(4,:)  = [ 2.5   2.0   0];
% SD.DetPos(5,:)  = [ 2.5   0.0   0];
% SD.DetPos(6,:)  = [ 2.5  -2.0   0];
% SD.DetPos(7,:)  = [ 0.5   2.0   0];
% SD.DetPos(8,:)  = [ 0.5   0.0   0];
% SD.DetPos(9,:)  = [ 0.5  -2.0   0];
% SD.DetPos(10,:) = [-0.5   2.0   0];
% SD.DetPos(11,:) = [-0.5   0.0   0];
% SD.DetPos(12,:) = [-0.5  -2.0   0];
% SD.DetPos(13,:) = [-2.5   2.0   0];
% SD.DetPos(14,:) = [-2.5   0.0   0];
% SD.DetPos(15,:) = [-2.5  -2.0   0];
% SD.DetPos(16,:) = [-4.5   2.0   0];
% SD.DetPos(17,:) = [-4.5   0.0   0];
% SD.DetPos(18,:) = [-4.5  -2.0   0];

%TODO #4:
```

```
%Generate the measurement list
% pairNUM = 0;
% for SrcIdx = 1 : 9      %size(SD.SrcPos,1)
%   for DetIdx = SrcIdx+1 : 9      %size(SD.DetPos,1)
%       temp1 = SD.SrcPos(SrcIdx,1:2);
%       temp2 = SD.DetPos(DetIdx,1:2);
%       ll = sqrt((temp1(1)-temp2(1))^2+(temp1(2)-temp2(2))^2);
%
%       if ll <= 3.0      %NN1=2.0cm; NN2=2.8cm
%          pairNUM = pairNUM + 1;
%          rr(pairNUM) = ll;
%          MeasList1(pairNUM,:) = [SrcIdx DetIdx 1 1];
%          MeasList2(pairNUM,:) = [SrcIdx DetIdx 1 2];
%       end
%    end
% end
% for SrcIdx = 10 : 18     %size(SD.SrcPos,1)
%   for DetIdx = SrcIdx+1 : 18      %size(SD.DetPos,1)
%       temp1 = SD.SrcPos(SrcIdx,1:2);
%       temp2 = SD.DetPos(DetIdx,1:2);
%       ll = sqrt((temp1(1)-temp2(1))^2+(temp1(2)-temp2(2))^2);
%
%       if ll <= 3.0      %NN1=2.0cm; NN2=2.8cm
%          pairNUM = pairNUM + 1;
%          rr(pairNUM) = ll;
%          MeasList1(pairNUM,:) = [SrcIdx DetIdx 1 1];
%          MeasList2(pairNUM,:) = [SrcIdx DetIdx 1 2];
%       end
%    end
% end
MeasList1 = [1 2  1 1;
  1 11  1 1;
  1 10  1 1;
  2 1   1 1;
  2 11  1 1;
  2 10  1 1;
  2 9   1 1;
  2 16  1 1;
  16 2  1 1;
  16 10 1 1;
  16 9  1 1;
  16 8  1 1;
  16 15 1 1;
  15 16 1 1;
  15 9 1  1;
  15 8 1  1;
  15 7 1  1;
  15 14 1 1;
  14 15 1 1;
  14 8  1 1;
```

```
14 7  1 1;
14 31 1 1;
14 12 1 1;
12 14 1 1;
12 7  1 1;
12 31 1 1;
11 1  1 1;
11 2  1 1;
11 10 1 1;
11 4  1 1;
11 5  1 1;
10 2  1 1;
10 1  1 1;
10 11 1 1;
10 5  1 1;
10 4  1 1;
10 3  1 1;
10 9  1 1;
10 16 1 1;
9 16  1 1;
9 2   1 1;
9 10  1 1;
9 4   1 1;
9 3   1 1;
9 32  1 1;
9 8   1 1;
9 15  1 1;
8 15  1 1;
8 16  1 1;
8 9   1 1;
8 3   1 1;
8 32  1 1;
8 6   1 1;
8 7   1 1;
8 14  1 1;
7 14  1 1;
7 15  1 1;
7 8   1 1;
7 32  1 1;
7 6   1 1;
7 30  1 1;
7 31  1 1;
7 12  1 1;
31 7  1 1;
31 12 1 1;
31 14 1 1;
31  6 1 1;
31 30 1 1;
5 11  1 1;
5 10  1 1;
```

```
5 4   1 1;
5 21  1 1;
5 22  1 1;
4 10  1 1;
4 11  1 1;
4 5   1 1;
4 22  1 1;
4 21  1 1;
4 20  1 1;
4 3   1 1;
4 9   1 1;
3 9   1 1;
3 10  1 1;
3 4   1 1;
3 21  1 1;
3 20  1 1;
3 19  1 1;
3 32  1 1;
3 8   1 1;
32 8  1 1;
32 9  1 1;
32 3  1 1;
32 20 1 1;
32 19 1 1;
32 18 1 1;
32 6  1 1;
32 7  1 1;
6 7   1 1;
6 8   1 1;
6 32  1 1;
6 19  1 1;
6 18  1 1;
6 29  1 1;
6 30  1 1;
6 31  1 1;
30 31 1 1;
30  7 1 1;
30  6 1 1;
30 18 1 1;
30 29 1 1;
22 27 1 1;
22 26 1 1;
22 21 1 1;
22 5  1 1;
22 4  1 1;
21 22 1 1;
21 27 1 1;
21 26 1 1;
21 25 1 1;
21 20 1 1;
```

```
21 3  1 1;
21 4  1 1;
21 5  1 1;
20 21 1 1;
20 26 1 1;
20 25 1 1;
20 24 1 1;
20 19 1 1;
20 32 1 1;
20 3  1 1;
20 4  1 1;
19 20 1 1;
19 25 1 1;
19 24 1 1;
19 23 1 1;
19 18 1 1;
19 3  1 1;
19 32 1 1;
19 6  1 1;
18 19 1 1;
18 24 1 1;
18 23 1 1;
18 28 1 1;
18 29 1 1;
18 30 1 1;
18 6  1 1;
18 32 1 1;
29  6 1 1;
29 18 1 1;
29 30 1 1;
29 28 1 1;
29 23 1 1;
27 22 1 1;
27 21 1 1;
27 26 1 1;
26 21 1 1;
26 22 1 1;
26 27 1 1;
26 25 1 1;
26 20 1 1;
25 20 1 1;
25 21 1 1;
25 26 1 1;
25 24 1 1;
25 19 1 1;
24 19 1 1;
24 20 1 1;
24 25 1 1;
24 23 1 1;
24 18 1 1;
```

```
23 18 1 1;
23 19 1 1;
23 24 1 1;
23 28 1 1;
23 29 1 1;
28 18 1 1;
28 23 1 1;
28 29 1 1;
13 12 1 1;
17 27 1 1];


MeasList2 = [1 2   1 2;
   1 11  1 2;
   1 10  1 2;
   2 1   1 2;
   2 11  1 2;
   2 10  1 2;
   2 9   1 2;
   2 16  1 2;
   16 2  1 2;
   16 10 1 2;
   16 9  1 2;
   16 8  1 2;
   16 15 1 2;
   15 16 1 2;
   15 9 1  2;
   15 8 1  2;
   15 7 1  2;
   15 14 1 2;
   14 15 1 2;
   14 8  1 2;
   14 7  1 2;
   14 31 1 2;
   14 12 1 2;
   12 14 1 2;
   12 7  1 2;
   12 31 1 2;
   11 1  1 2;
   11 2  1 2;
   11 10 1 2;
   11 4  1 2;
   11 5  1 2;
   10 2  1 2;
   10 1  1 2;
   10 11 1 2;
   10 5  1 2;
   10 4  1 2;
```

```
10 3  1 2;
10 9  1 2;
10 16 1 2;
9 16  1 2;
9 2   1 2;
9 10  1 2;
9 4   1 2;
9 3   1 2;
9 32  1 2;
9 8   1 2;
9 15  1 2;
8 15  1 2;
8 16  1 2;
8 9   1 2;
8 3   1 2;
8 32  1 2;
8 6   1 2;
8 7   1 2;
8 14  1 2;
7 14  1 2;
7 15  1 2;
7 8   1 2;
7 32  1 2;
7 6   1 2;
7 30  1 2;
7 31  1 2;
7 12  1 2;
31 7  1 2;
31 12 1 2;
31 14 1 2;
31  6 1 2;
31 30 1 2;
5 11  1 2;
5 10  1 2;
5 4   1 2;
5 21  1 2;
5 22  1 2;
4 10  1 2;
4 11  1 2;
4 5   1 2;
4 22  1 2;
4 21  1 2;
4 20  1 2;
4 3   1 2;
4 9   1 2;
3 9   1 2;
3 10  1 2;
3 4   1 2;
3 21  1 2;
3 20  1 2;
```

```
3 19  1 2;
3 32  1 2;
3 8   1 2;
32 6  1 2;
32 7  1 2;
32 8  1 2;
32 9  1 2;
32 3  1 2;
32 20 1 2;
32 19 1 2;
32 18 1 2;
6 7   1 2;
6 8   1 2;
6 32  1 2;
6 19  1 2;
6 18  1 2;
6 29  1 2;
6 30  1 2;
6 31  1 2;
30 31 1 2;
30  7 1 2;
30  6 1 2;
30 18 1 2;
30 29 1 2;
22 27 1 2;
22 26 1 2;
22 21 1 2;
22 5  1 2;
22 4  1 2;
21 22 1 2;
21 27 1 2;
21 26 1 2;
21 25 1 2;
21 20 1 2;
21 3  1 2;
21 4  1 2;
21 5  1 2;
20 21 1 2;
20 26 1 2;
20 25 1 2;
20 24 1 2;
20 19 1 2;
20 32 1 2;
20 3  1 2;
20 4  1 2;
19 20 1 2;
19 25 1 2;
19 24 1 2;
19 23 1 2;
19 18 1 2;
```

```
19 3  1 2;
19 32 1 2;
19 6  1 2;
18 19 1 2;
18 24 1 2;
18 23 1 2;
18 28 1 2;
18 29 1 2;
18 30 1 2;
18 6  1 2;
18 32 1 2;
29  6 1 2;
29 18 1 2;
29 30 1 2;
29 28 1 2;
29 23 1 2;
27 22 1 2;
27 21 1 2;
27 26 1 2;
26 21 1 2;
26 22 1 2;
26 27 1 2;
26 25 1 2;
26 20 1 2;
25 20 1 2;
25 21 1 2;
25 26 1 2;
25 24 1 2;
25 19 1 2;
24 19 1 2;
24 20 1 2;
24 25 1 2;
24 23 1 2;
24 18 1 2;
23 18 1 2;
23 19 1 2;
23 24 1 2;
23 28 1 2;
23 29 1 2;
28 18 1 2;
28 23 1 2;
28 29 1 2;
13 12 1 2;
17 27 1 2];


SD.MeasList = [MeasList1; MeasList2];
clear MeasList1 MeasList2;
```

```matlab
%TODO #5:
% Specify the raw data from DyNot
fs = 1.81;
Source = 1:32;
Detector= 1:32;
fn = sprintf('%s.wl1',fid);
WL1 = load(fn,'-ascii');
fn = sprintf('%s.wl2',fid);
WL2 = load(fn,'-ascii');
clear fn;

%TODO #6: Pre-process DyNot data
%Remove negtive speckles
[a b] = find(WL1<=0);
for i = 1:length(a)
   if a(i) == 1
      WL1(a(i),b(i)) = abs(WL1(a(i),b(i)));
   else
      WL1(a(i),b(i)) = WL1(a(i)-1,b(i));
   end
end
clear a b;
[a b] = find(WL2<=0);
for i = 1:length(a)
   if a(i) == 1
      WL2(a(i),b(i)) = abs(WL2(a(i),b(i)));
   else
      WL2(a(i),b(i)) = WL2(a(i)-1,b(i));
   end
end
clear a b;


%TODO #7:
% Specify the raw data for selected S-D pairs
pairNUM = size(SD.MeasList,1)/2;
for idx = 1 : pairNUM
   SelectSrc = SD.MeasList(idx,1);
   SelectDet = SD.MeasList(idx,2);
      d(:,idx)        = WL1(:,(SelectSrc-1)*length(Detector)+SelectDet);
      d(:,idx+pairNUM) = WL2(:,(SelectSrc-1)*length(Detector)+SelectDet);

%   d(:,idx)        = sqrt(WL1(:,(SelectSrc-1)*length(Detector)+SelectDet).*WL1(:,(SelectDet-
1)*length(Detector)+SelectSrc));
%   d(:,idx+pairNUM) = sqrt(WL2(:,(SelectSrc-
1)*length(Detector)+SelectDet).*WL2(:,(SelectDet-1)*length(Detector)+SelectSrc));
end
clear idx1 SelectSrc SelectDet;
```

```
%TODO #8:
ml=SD.MeasList;
[DataLength y] = size(d);
t = (1:DataLength)/fs;
s = zeros(size(t));
aux10 = zeros(size(t));

fileout = sprintf( '%s.nirs', fid);
save(fileout,'t','d','s','aux10','ml','SD','-MAT');
```

APPENDIX B

ADAPTIVE FILTERING MATLAB CODE

```
fs = 1.81;
filenm = 'NiRs File'
load NIrs File.nirs -mat

d_old = d;
[row,column] = size(d);
Right = round((column/2 - 2)/2);
Lambda1R = FiltSig(d(:,1:Right),fs);
Lambda1L = FiltSig(d(:,Right+1:Right*2),fs);

Right2B = round(column/2 + 1);
Right2E = (column/2 - 2 - Right2B)/2;
Lambda2R = FiltSig(d(:,Right2B:Right2B+Right-1),fs);
Lambda2L = FiltSig(d(:,Right2B+Right:column-2),fs);

Noise_Lambda1R = FiltSig(d(:,column/2-1),fs);
Noise_Lambda1L = FiltSig(d(:,column/2),fs);
Noise_Lambda2R = FiltSig(d(:,column-1),fs);
Noise_Lambda2L = FiltSig(d(:,column),fs);

colcount = 1;
[row1R,col1R] = size(Lambda1R);
while colcount < col1R + 1
    Lags1R = FindLag(fs,Lambda1R(:,colcount),Noise_Lambda1R,'Resp');
    [Lambda1R_pad, Resp_pad] = Resp_Padding(Lambda1R(:,colcount), Noise_Lambda1R,
Lags1R);
    [Lambda1R_Clean(:,colcount), Error_C(:,colcount)] =
AdaptiveFilterResp(Lambda1R_pad, Resp_pad, Lags1R);
    colcount = colcount + 1;
end
colcount = 1;
[row1L,col1L] = size(Lambda1L);
while colcount < col1L + 1
    Lags1L = FindLag(fs,Lambda1L(:,colcount),Noise_Lambda1L,'Resp');
    [Lambda1L_pad, Resp_pad] = Resp_Padding(Lambda1L(:,colcount), Noise_Lambda1L,
Lags1L);
    [Lambda1L_Clean(:,colcount), Error_C(:,colcount)] = AdaptiveFilterResp(Lambda1L_pad,
Resp_pad, Lags1L);
    colcount = colcount + 1;
end
colcount = 1;
[row2R,col2R] = size(Lambda2R);
while colcount < col2R + 1
    Lags2R = FindLag(fs,Lambda2R(:,colcount),Noise_Lambda2R,'Resp');
    [Lambda2R_pad, Resp_pad] = Resp_Padding(Lambda2R(:,colcount), Noise_Lambda2R,
Lags2R);
    [Lambda2R_Clean(:,colcount), Error_C(:,colcount)] =
AdaptiveFilterResp(Lambda2R_pad, Resp_pad, Lags2R);
    colcount = colcount + 1;
end
```

```
colcount = 1;
[row2L,col2L] = size(Lambda2L);
while colcount < col2L + 1
    Lags2L = FindLag(fs,Lambda2L(:,colcount),Noise_Lambda2L,'Resp');
    [Lambda2L_pad, Resp_pad] = Resp_Padding(Lambda2L(:,colcount), Noise_Lambda2L,
Lags2L);
    [Lambda2L_Clean(:,colcount), Error_C(:,colcount)] = AdaptiveFilterResp(Lambda2L_pad,
Resp_pad, Lags2L);
    colcount = colcount + 1;
end
d = [Lambda1R_Clean Lambda1L_Clean Noise_Lambda1R Noise_Lambda1L
Lambda2R_Clean Lambda2L_Clean Noise_Lambda2R Noise_Lambda2L];
for c = 1:column
    Old = d_old(:,c);
    d(:,c) = d(:,c) + mean(Old(:));
end
newfile = sprintf('%s_Filt.nirs', filenm);
save(newfile,'t','d','s','aux10','ml','SD','-MAT');

% while colcount < column + 1
%     NIRS_Clean(:,colcount) = NIRS_Clean(:,colcount) - mean(d_old(:,colcount)); % Do
this when all filtering is done
%     colcount = colcount + 1;
% end
%
% colcount = 1;
% NIRS_PCA_Clean1(:,1:28) = PCA(NIRS_Clean(:,1:28), NIRS_Clean(1:400,1:28),1);
% NIRS_PCA_Clean1(:,29:56) = PCA(NIRS_Clean(:,29:56), NIRS_Clean(1:400,29:56),1);
% while colcount < column + 1
%     NIRS_PCA_Clean1(:,colcount) = NIRS_PCA_Clean1(:,colcount) +
mean(d_old(:,colcount)); % Do this when all filtering is done
%     colcount = colcount + 1;
% end
%
% d = NIRS_PCA_Clean1;
% newfile = sprintf('%s_RPad_RC_PCA1afterFilt20hz.nirs', filenm);
% save(newfile,'t','d','s','aux10','ml','SD','-MAT');
%
% colcount = 1;
% NIRS_PCA_Clean2(:,1:28) = PCA(NIRS_Clean(:,1:28), NIRS_Clean(1:400,1:28),2);
% NIRS_PCA_Clean2(:,29:56) = PCA(NIRS_Clean(:,29:56), NIRS_Clean(1:400,29:56),2);
% while colcount < column + 1
%     NIRS_PCA_Clean2(:,colcount) = NIRS_PCA_Clean2(:,colcount) +
mean(d_old(:,colcount)); % Do this when all filtering is done
%     colcount = colcount + 1;
% end
%
% d = NIRS_PCA_Clean2;
% newfile = sprintf('%s_RPad_RC_PCA2afterFilt20hz.nirs', filenm);
% save(newfile,'t','d','s','aux10','ml','SD','-MAT');
```

```
%
% colcount = 1;
% NIRS_PCA_Clean3(:,1:28) = PCA(NIRS_Clean(:,1:28), NIRS_Clean(1:400,1:28),3);
% NIRS_PCA_Clean3(:,29:56) = PCA(NIRS_Clean(:,29:56), NIRS_Clean(1:400,29:56),3);
% while colcount < column + 1
%     NIRS_PCA_Clean3(:,colcount) = NIRS_PCA_Clean3(:,colcount) +
mean(d_old(:,colcount)); % Do this when all filtering is done
%     colcount = colcount + 1;
% end
%
% d = NIRS_PCA_Clean3;
% newfile = sprintf('%s_RPad_RC_PCA3afterFilt20hz.nirs', filenm);
% save(newfile,'t','d','s','aux10','ml','SD','-MAT'); clear all
```

APPENDIX C

SPATIOTEMPORAL MATLAB CODE

```matlab
function [Ca, Cd, Ct] = Cluster(Image, K, max_iter, Base, Act, Dur, Fs)
%% The purpose of this function is to cluster pixels with similar temporal
%% patterns. At the end each cluster mean is undergoes statistical analysis
%% to determine whether that cluster of pixels consisted of activation or
%% not.

%% Inputs:
% Image: A set of images for every time point
% K: Number of clusters for activation. This number is later doubled to
% also look for deactivated pixels.
% max_iter: is the max iteration

%% Outputs:
% Ca: Image with potential activated pixels assigned their cluster number
% Cd: Image with potential deactivated pixels assigned their cluster number
% Ct: Image with the p-values for each cluster

K = 2*K + 1;
Act = round((Act)*Fs);
Act1 = Act+1:2*Act;
Act2 = 2*Act+1:3*Act;
Act3 = 3*Act+1:4*Act;
Act4 = 4*Act+1:5*Act;
Act5 = 5*Act+1:6*Act;
Act6 = 6*Act+1:7*Act;
Dur = round(Dur*Fs);
Act = Act(Dur:end);
Base = round(Base*Fs);
Base = 1:Base;

[row, column, time] = size(Image);

%% This line is for the DYNOT data with 32 source/detectors.
HRF = Gamma(time,max(Base),Dur,Fs);


%% These four lines are for the CP data with CW5 setup. Use the
%% third line for the first round (Subj 1 to Subj 11), and the fourth line
%% for second round (Subj 12 to Subj 32).
% Base = 1:50;
% Act = 151:200;
% HRF = Gamma(351,150,10);
% HRF = Gamma(451,150,10);


HRF = HRF/max(HRF);
% Ca = zeros(row, column);
% Cd = zeros(row, column);
C = zeros(row, column);
Cmeanold = zeros(time, K);
```

```matlab
m = round((K+1)/2);

%% Initialize the cluster means
Cmeanold(:,1) = max(Image(:)).*HRF;
Cmeanold(:,m) = zeros(time,1);
Cmeanold(:,K) = min(Image(:)).*HRF;
kcnt = zeros(K,1);
for k = 2:m-1
    Cmeanold(:,k) = Cmeanold(:,1)/k;
end
for k = m+1:K-1
    Cmeanold(:,k) = Cmeanold(:,K)/((K-1)/(2*(k-m)));
end
d = zeros(K,1);

%% Cluster the pixels
for iter=1:max_iter
    Cmean = zeros(time, K);
    for r=1:row
        for c=1:column
            sig = Image(r,c,:);
            for k=1:K
                d(k) = newdistfcm(Cmeanold(:,k),sig(:),2,0.4);
%                 if isnan(d(k))
%                     U = 'what?'
%                 end
            end
            mind = min(d);
            for k=1:K
                if mind == d(k)
                    C(r,c) = k;
                    Cmean(:,k) = Cmean(:,k)+sig(:);
                    kcnt(k) = kcnt(k) + 1;
                end
            end
        end
    end
    for k=1:K
        Cmean(:,k) = Cmean(:,k)/kcnt(k);
        kcnt(k) = 0;
    end
    if Cmean == Cmeanold
        break;
    else
        Cmeanold = Cmean;
    end
end

%% Seperate the possible active pixels from the possible deactivated
%% pixels by cluster.
```

```
Ca = C;
Cd = C;
for k=1:K
    figure, hold on,
    for r=1:row
        for c=1:column
            if C(r,c) == k
                sig = Image(r,c,:);
                maxs = max(max(sig(:)), abs(min(sig(:))));
%                if (max(sig(:)/maxs) < 1) || (max(sig(:)) == abs(min(sig(:)))) || (C(r,c) > m)
                if (max(sig(:)/maxs) < 1) || (C(r,c) > m)
                    Ca(r,c) = 0;
                else
%                    plot(sig(:)/maxs);
                    plot(sig(:));
                end
%                if (min(sig(:)/maxs) > -1) || (max(sig(:)) == abs(min(sig(:)))) || (C(r,c) < m)
                if (min(sig(:)/maxs) > -1) || (C(r,c) < m)
                    Cd(r,c) = 0;
                else
%                    plot(sig(:)/maxs);
                    plot(sig(:));
                end
            end
        end
    end
    plot(Cmean(:,k),'r');
    hold off
end

%% Perform statistical analysis of each cluster mean.
Ct = zeros(size(C),6);
tres = zeros(size(d),6);
for k=1:K
    if ~isnan(d(k));
        [h,p] = ttest2(Cmean(Base,k),Cmean(Act1,k),[],[],'unequal');
        tres(k,1) = p;
        [h,p] = ttest2(Cmean(Base,k),Cmean(Act2,k),[],[],'unequal');
        tres(k,2) = p;
        [h,p] = ttest2(Cmean(Base,k),Cmean(Act3,k),[],[],'unequal');
        tres(k,3) = p;
        [h,p] = ttest2(Cmean(Base,k),Cmean(Act4,k),[],[],'unequal');
        tres(k,4) = p;
        [h,p] = ttest2(Cmean(Base,k),Cmean(Act5,k),[],[],'unequal');
        tres(k,5) = p;
        [h,p] = ttest2(Cmean(Base,k),Cmean(Act6,k),[],[],'unequal');
        tres(k,6) = p;
    end
end
```

```
%% Save the p-values into an image.
for k=1:K
    for r=1:row
        for c=1:column
            if C(r,c) == k
                Ct(r,c,1) = tres(k,1);
                Ct(r,c,2) = tres(k,2);
                Ct(r,c,3) = tres(k,3);
                Ct(r,c,4) = tres(k,4);
                Ct(r,c,5) = tres(k,5);
                Ct(r,c,6) = tres(k,6);
            end
        end
    end
end
figure, plot(1:K,tres);
return
```

APPENDIX D

DYNOT SPECIFICATIONS

Light Sources:
Type ....Laser diodes
Illumination power (average, per wavelength) ....20 mW
Illumination radiance (per wavelength) ....2.5 mJ cm-2sr-2
Number of wavelengths...2 to 4 (frequency-encoded)
Wavelength range..680 nm to 900 nm
Modulation...4-12 kHz, sine-wave
Number of illumination positions...............................1 to 32
Source switching rate..60 Hz
Illumination variation...<1%
Laser Class...1

Detection:
Detector type ....Silicon photodiode, 2.4 mm × 2.4 mm
Number of detection channels 32
Sensitivity...<10 pW
Dynamic range ....7×10^8
Long-term stability..1% (30 minutes)
Data acquisition rate ....2 Hz (full tomographic) 70 Hz
(single-source, fast scan mode)

Electrical:
Input voltage ....110 VAC (American model) 220-
240VAC (International model)
Power consumption (max)..1500 W
Frequency...50 Hz to 60 Hz
Phases..1

Environmental:
Temperature range..10°C to 40°C (operating) -15°C
                                                                                    to+70°C (storage and transport)
Humidity..20 to 80% relative humidity noncondensing
Ambient pressure..700 hPa to 1060 hPa

General:
Overall physical dimensions (W × D × H) ....41.0" × 29.0" × 39.5" (1040 mm
× 740 mm × 1000 mm)
Weight ....400 lbs
Certification..…….CE pending (European model)
Classification:
Degree of electric shock protection ....Class 1
Type of electric shock protection................................Type BF
Degree of protection against the
ingress of liquids………………….….............................IPX 0 (not protected)
Mode of operation ....Continuous

REFERENCES

[1]   T. J. Huppert, R. D. Hoge, A. M. Dale, M. A. Franceschini, D. A Boas, "Quantitative spatial comparison of diffuse optical imaging with blood oxygen level-dependent and arterial spin labeling-based functional magnetic resonance imaging " *Journal of Biomedical Optics,* vol. 11, 2006.

[2]   "S. Bunce, M. Izzetoglu, K. Izzetoglu, B. Onaral, and K. Pourrezaei, "Functional Near-Infrared Spectroscopy," IEEE Engineering in Medicine and Biology Magazine, pp. 54-61, 2006.

[3]   D. Boas, "Near infrared imaging," *Scholarpedia,* vol. 4, 2009.

[4]   A. Bozkurt, B. Onaral, "Safety assessment of near infrared light emitting diodes for diffuse optical measurements," BioMedical *Engineering OnLine,* vol. 3, 2004.

[5]   M. Izzetoglu, S. Bunce, H. Ayaz, A. Devaraj, B. Onaral, K. Pourrezaei, "Functional near-infrared neuroimaging," *IEEE Transactions on Neural Systems and Rehabilitation Engineering,* vol. 13, pp. 153-159, June 2005

[6]   B. Chance, M. Cope, E. Gratton, N. Ramanujam, and B. Tromberg, "Phase measurement oflight absorption and scatter in human tissue," Review of Scientific Instruments, vol. 69(10),pp. 3457-3481, 1998

. [7]   G. Strangman, J. P. Culver, J. H. Thompson, D. A Boas, "A Quantitative Comparison of Simultaneous BOLD fMRI and NIRS Recordings during Functional Brain Activation," *NeuroImage,* vol. 17, pp. 719-731, October 2002.

[8]   T. Q. D. Khoa, M. Nakagawa, "Recognizing brain activities by functional near-infrared spectroscope signal analysis," *Nonlinear Biomed Phys,* vol. 2, July 2008.

[9]   D. T. Stuss, M. P. Alexander, "Executive functions and the frontal lobes: a conceptual view," *Psychological Research,* vol. 63, pp. 289-298, August 2000.

[10]   J. K. Mai, G. Paxinos, J. K. Assheuer, *Atlas of the Human Brain*, 3 ed. Amsterdam: Elsevier Academic Press, 2008.

[11]   Y. Yang, A. Raine, "Prefrontal structural and functional brain imaging findings in antisocial, violent, and psychopathic individuals: A meta-analysis," *Psychiatry Research,* vol. 174, pp. 81-88, November 2009.

[12]   MA Franceschini, S. Fantini., JH Thompson., J.P. Culver, D.A.Boas., "Hemodynamic evoked response of the sensorimotor cortex measured non-invasively with near-infrared optical imaging. Psychophysiology" 42 (16), 3063– 3072, 2003.

[13]   I. M. Mihara, M. Hatakenaka, K. Kubota, S. Sakoda, "Role of the prefrontal cortex in human balance control," *NeuroImage,* vol. 43, pp. 329-336, November 2008.

[14]   T. F. B. Khan, K. Behbehani, M. I. Romero, M. R. Delgado, N. J. Clegg, L. Smith , D. Reid, H. Liu, G. Alexandrakis, "Identification of abnormal motor cortex activation patterns in children with cerebral palsy by functional near-infrared spectroscopy," *Journal of Biomedical Optics,* vol. 15, June 2010.

[15]   M. R. Delgado; M. I. Romero; F. Tian; B. Kahn; G. Alexandrakis, H. Liu, "Early Bilateral Cortical Activation in Children with Subcortical Hemiplegic Cerebral Palsy Revealed by NIRS," in *AACPDM* Scottsdale, Arizona, 2010.

[16]   B. R. White, A. L. Cohen, S. E. Petersen, M. E. Raichle, "Resting-state functional connectivity in the human brain revealed with diffuse optical tomography," *NeuroImage,* vol. 47, pp. 148-156, August 2009.

[17]   A. H. Hielscher, G. S. Abdoulaev, A. D. Klose, J. Lasker, M. Stewart, U. Netz, J. Beuthan, "Near-infrared diffuse optical tomography," *Disease Markers,* vol. 18, pp. 313-337, February 2004.

[18]   H. L. G. Christoph, H. Schmitz, H. Luo, I. Arif, J. Hira, Y. Pei, A. Bluestone, S. Zhong, R. Andronica, I. Soller, N. Ramirez, S. Barbour, R. L. Barbour, "Instrumentation and Calibration

Protocol for Imaging Dynamic Features in Dense-Scattering Media by Optical Tomography," *Applied Optics,* vol. 39, pp. 6466-6486, December 2000.

[19]   "Dynot User Manual." NIRX Medical Technologies, 2003

[20]   C. Goetz, *Textbook of Clinical Neurology*, 3rd ed.: Saunders, 2007.

[21]   D. A. Purves, J. George, Fitzpatrick, David, Katz, C. Lawrence, LaMantia, A. Samuel, McNamara, O. James, Williams, S. Mark, *Neuroscience*, 2nd ed. Sunderland, MA: Sinauer Associates, Inc., 2001.

[22]   D. J. Roth, M. Raybaudi, R. Massarelli, C. D. Martin, C. Segebarth, S. Morand, A. Gemignani, M. Décorps, M. Jeannerod, "Possible involvement of primary motor cortex in mentally simulated movement: a functional magnetic resonance imaging study," *Neuroreport,* vol. 17, pp. 1280-1284, May 1996.

[23]   T. R. Wilder Penfield, *The Cerebral Cortex of Man: A Clinical Study of Localization of Function.* New York: Macmillan, 1968.

[24]   R. A. B. Adel, K. Afifi, *Functional neuroanatomy: text and atlas* 2nd ed. Iowa City, IA: McGraw-Hill Medical, 2005.

[25]   K. Gugleta, G. Fuchsjäger-Mayrl, S. Orgül, "Is Neurovascular Coupling of Relevance in Glaucoma?" *SURVEY OF OPHTHALMOLOGY,* vol. 52, pp. 139-143, November 2007.

[26]   V. V. Tuchin, *Handbook of optical biomedical diagnostics*, 1 ed. Bellingham: SPIE Publications, 2002.

[27]   Y. Hoshi, "Functional near-infrared optical imaging: Utility and limitations in human brain mapping," *Psychophysiology,* vol. 40, pp. 511–520, June 2003.

[28]   D. F. James, G. Fujimoto, L. Daniel, Farkas, *Biomedical Optical Imaging*, 1 ed. USA: Oxford University Press, 2009.

[29]   H. W. J Steinbrink, H. Obrig, A. Villringer, H. Rinneberg, "Determining changes in NIR absorption using a layered model of the human head," *Physics in Medicine and Biology* vol. 46, pp. 879-896, March 2001.

[30]   Popov, J. Lademann, R. Myllylä, "Advantages of NIR radiation use for optical determination of skin horny layer thickness with embedded TiO2 nanoparticles during tape stripping procedure," *LASER METHODS IN BIOLOGY AND MEDICINE,* vol. 16, pp. 751-757, December 2006.

[31]   D. T. Delpy, M. Cope, P. van der Zee, S. Arridge, S. Wray, J. Wyatt, "Estimation of optical pathlength through tissue from direct time of flight measurement," *Physics in Medicine and Biology,* vol. 33, pp. 1433-1442, December 1988.

[32]   K. D. Clarke, *An Illustrated History of Brain Function: Imaging the Brain from Antiquity to the Present* 3rd ed.: Norman Neurosciences Series, 1996.

[33]   M. A. Franceschini, D. K. Joseph, T. J. Huppert, S. G. Diamond, D. A. Boas, "Diffuse optical imaging of the whole head," *Journal of Biomedical Optics,* vol. 11, p. 054007, October 2006.

[34]   J. C. Francois, G. Meyer, "Spatiotemporal clustering of fMRI time series in the spectral domain," *Medical Image Analysis,* vol. 9, pp. 51-68, February 2005.

[35]   A. Devaraj, "Signal processing for functional near-infrared neuroimaging " Master of Science, Electrical Engineering, Drexel University, Philadelphia June 2005.

[36]   M. F. T. Sutoa, M. Itoa, T. Ueharaa, M. Mikunia, "Multichannel near-infrared spectroscopy in depression and schizophrenia: cognitive brain activation study," *Biological Psychiatry,* vol. 55, pp. 501-511, March 2004.

[37]   F. Y. Sato, M. Kiguchi, T. Katura , A. Maki, T. Yoro, H. Koizumi, "Intersubject variability of near-infrared spectroscopy signals during sensorimotor cortex activation," *Journal of Biomedical Optics,* vol. 10, p. 44001, August 2005.

76

[38]   M. W. G. Morren, P. Lemmerling, U. Wolf, J. H. Choi, E. Gratton, L. De Lethauwer, S. Van Huffel,, "Detection of fast neural signals in the motor cortex from function near infrared spectroscopy measurements using independent component analysis," *Medical and Biological Engineering and Computing,* vol. 42, pp. 92-99, 2004.

[39]   Wilcox T, Bortfeld H, Woods R, Wruck E, Boas DA. "Using near-infrared spectroscopy to assess neural activation during object processing in infants. J Biomed Opt. 2005; 10:11010

[40]   F. G. Meyer, J. Chinrungrueng, "Spatiotemporal clustering of fMRI time series in the spectral domain," *Medical Image Analysis,* vol. 9, pp. 51-68, February 2005.

[41]   R. C. Mesquita, D. A. Boas, "Resting state functional connectivity of the whole head with near-infrared spectroscopy," *Biomedical Optics Express,* vol. 1, pp. 324-336, 2010.

[42]   Cope M, Delpy DT, Reynolds EO, Wray S, Wyatt J, van der Zee P." Methods of quantitating cerebral near infrared spectroscopy data". Adv Exp Med Biol. 1988;222:183–189

[43]   G. Morren, M. Wolf, P. Lemmerling, U. Wolf, J.H. Choi, E. Gratton, L. De Lethauwer, and S. Van Huffel, "Detection of fast neural signals in the motor cortex from function near infrared spectroscopy measurements using independent component analysis," Med. Biol. Eng. Comput., vol. 42, pp. 92-99, 2004.

[44]   B. Khan, K. Behbehani, M. I. Romero, M. R. Delgado, N. J. Clegg, L. Smith, D. Reid, H. Liu, G. Alexandrakis, "Identification of abnormal motor cortex activation patterns in children with cerebral palsy by functional near-infrared spectroscopy," *Journal of Biomedical Optics,* vol. 15, June 2010

[45]   E. R. Kandel, T. M. Jessell, *Principles of neural science*, 4th ed.: McGraw-Hill, 2000.

[46]   D. J. D. Kâmil Uludağ , E. J. Yodera, K. Restoma, T. Liua, R. Buxtona, "Coupling of cerebral blood flow and oxygen consumption during physiological activation and deactivation measured with fMRI," *NeuroImage,* vol. 23, pp. 148-155, September 2004.

[47]   F. P. Matthews, B.A. Ward, T.E. Soraghan, C. Markham, "Hemodynamics for Brain-Computer Interfaces," *Signal Processing Magazine, IEEE* vol. 25, pp. 87 – 94, 2008.

[48]   M. A. Franceschini, S. Fantini, V. Toronov, M. E. Filiaci, and E. Gratton, "Cerebral hemodynamics measured by near-infrared spectroscopy at rest and during motor activation," Proceedings of Inter-Institute Workshop on in Vivo Optical Imaging at the Nih, 73-80 213 (2000).

[49]   B. Khan, "Functional Near Infrared Spectroscopy For The Assessment Of Motor Cortex Plasticity In Pediatric Subjects Affected By Cerebral Palsy," Master of Science, Biomedical Engineering, University Of Texas At Arlington, Arlington August 2009.

[50]   D. D. Cope, E. O. Reynolds, S. Wray, J. Wyatt, P. van der Zee, "Methods of quantitating cerebral near infrared spectroscopy data," *Adv Exp Med Biol,* vol. 222, pp. 183–189, 1988.

[51]   A. Sassaroli, S. Fantini, "Comment on the modified Beer–Lambert law for scattering media," *Physics in Medicine and Biology,* vol. 49, 2004.

[52]   H. P. Kocsis, A. Eke, "The modified Beer–Lambert law revisited," Phys Med Biol*,* vol. 51, pp. N91–N98, 2006.

[53]   C. D. Gaetz, "Localization of sensorimotor cortical rhythms induced by tactile stimulation using spatially filtered MEG," *Neuroimage,* vol. 30, pp. 899-908, April 2006.

[54]   A. K. Dionyssios Mintzopoulos, A. Konstas, L. G. Astrakas, A. B. Singhal, M. A. Moskowitz, B. R. Rosen, A. Tzika, "Functional MRI of Rehabilitation in Chronic Stroke Patients Using Novel MR-Compatible Hand Robots," *Open Neuroimag J,* vol. 2, pp. 94-101, September 2008.

[55]   T Huppert, D A. Boas "HOMER Manual- NIRS data analysis GUI" July 28, 2005

[56]   Rickson C. Mesquita, Maria A. Franceschini and David A. Boas , "Resting state functional connectivity of the whole head with near-infrared spectroscopy"

[57]   Bharat Biswal, F. Zerrin Yetkin, Victor M. Haughton, James S. Hyde, "Functional Connectivity in the Motor Cortex of Resting Human Brain Using Echo-Planar MRI"

[58]   Stefan P. Koch1, Christina Habermehl, Jan Mehnert, Christoph H. Schmitz, Susanne Holtze, Arno Villringer, Jens Steinbrink and Hellmuth Obrig "High-resolution optical functional mapping of the human somatosensory cortex"

BIOGRAPHICAL INFORMATION

Pankaj Chand was born on August 21, 1983 in Pithoragarh (Uttaranchal), India. He secured his Bachelor of Engineering Degree in Biomedical Engineering from Mumbai University, India in July 2005. He worked for three years in biomedical industry from 2005-2008. From Fall-2008 he started his graduate studies in Biomedical Engineering from joint program of Biomedical Engineering at the University of Texas at Arlington and University of Texas Southwestern Medical Center at Dallas. His research expertise is in medical imaging and image processing.